

# Slip on the San Andreas Fault at Parkfield, California, over Two Earthquake Cycles, and the Implications for Seismic Hazard

by Jessica Murray and John Langbein

**Abstract** Parkfield, California, which experienced  $M$  6.0 earthquakes in 1934, 1966, and 2004, is one of the few locales for which geodetic observations span multiple earthquake cycles. We undertake a comprehensive study of deformation over the most recent earthquake cycle and explore the results in the context of geodetic data collected prior to the 1966 event. Through joint inversion of the variety of Parkfield geodetic measurements (trilateration, two-color laser, and Global Positioning System), including previously unpublished two-color data, we estimate the spatial distribution of slip and slip rate along the San Andreas using a fault geometry based on precisely relocated seismicity.

Although the three most recent Parkfield earthquakes appear complementary in their along-strike distributions of slip, they do not produce uniform strain release along strike over multiple seismic cycles. Since the 1934 earthquake, more than 1 m of slip deficit has accumulated on portions of the fault that slipped in the 1966 and 2004 earthquakes, and an average of 2 m of slip deficit exists on the 33 km of the fault southeast of Gold Hill to be released in a future, perhaps larger, earthquake. It appears that the fault is capable of partially releasing stored strain in moderate earthquakes, maintaining a disequilibrium through multiple earthquake cycles. This complicates the application of simple earthquake recurrence models that assume only the strain accumulated since the most recent event is relevant to the size or timing of an upcoming earthquake. Our findings further emphasize that accumulated slip deficit is not sufficient for earthquake nucleation.

*Online material:* Model fault geometry, fit to the data for the inversions, and model resolution.

## Introduction

Parkfield, California, has become well-known for its series of six magnitude  $\sim 6$  earthquakes, the most recent of which took place 28 September 2004. Prior to the 2004 event, Parkfield earthquakes were often cited for their similarities, which included epicenters near Middle Mountain (Fig. 1), southeastward rupture propagation, strikingly similar seismograms and, for the 1934 and 1966 events, identical foreshocks. The average 22-year recurrence interval led to the unfulfilled prediction that another Parkfield earthquake would occur in 1988 (Bakun and Lindh, 1985). The 2004  $M$  6.0 earthquake was similar to previous Parkfield events in terms of the aftershock distribution and extent of surface cracking. However, it was different in several ways, for instance, in the character of its waveforms and its lack of foreshocks (Langbein *et al.*, 2005). Notably, the hypocenter of the 2004 earthquake was beneath Gold Hill (Fig. 1), 20 km southeast of Middle Mountain, and its rupture propagated to the northwest.

Before the Parkfield Earthquake Prediction Experiment of the 1980s (Bakun and Lindh, 1985), and even before the  $M$  6.0 Parkfield earthquake in 1966, geodetic data were collected along the San Andreas fault (SAF) in this region. With measurements back to 1923, Parkfield is one of the few places on Earth for which geodetic data provide a means of imaging strain accumulation and release on the fault through the earthquake cycle. The SAF near Parkfield is a transitional zone between the creeping section to the northwest, which slips steadily at a rate of 25–30 mm/yr (Burford and Harsh, 1980; Lisowski and Prescott, 1981; Titus *et al.*, 2005), and the locked section to the southeast, which last ruptured in the 1857  $M_w$  7.9 Fort Tejon earthquake (Sieh, 1978). The geodetic observations made here are critical to our understanding of long-term earthquake hazard and the potential for spatiotemporal variability in strain accumulation in this region.

Several studies have used geodetic data to investigate

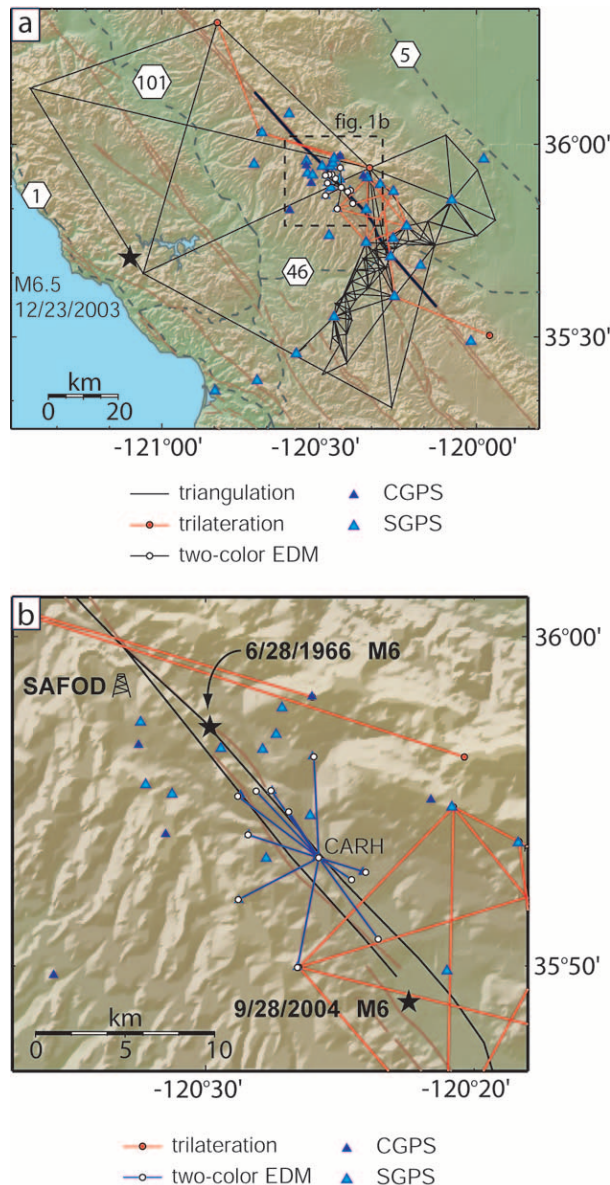


Figure 1. Geodetic networks in the Parkfield, California, area that have observations for the coseismic and/or postseismic periods of the 1934, 1966, and 2004 earthquakes. Faults are shown in brown; dashed gray lines are major highways marked with their route numbers. (a) Parkfield region. The heavy black line is the surface trace of the primary model fault surface; the subsidiary SWFZ surface trace is not shown here for figure clarity (see Fig. 1b, 3a). 23 December 2003 M 6.5 San Simeon earthquake shown by star. (b) Close-up of Parkfield area. Stars mark the 1966 earthquake (at Middle Mountain) and the 2004 earthquake epicenters. Gold Hill is located on the east side of the fault opposite the star marking the 2004 event. Note bend in the fault southeast of Gold Hill. SAFOD, San Andreas Fault Observatory at Depth scientific borehole.

coseismic slip and interseismic creep at Parkfield during various time intervals. For example, through inversion of line-length measurements from a regional trilateration network, Segall and Harris (1987) inferred that the peak slip in the 1966 earthquake was concentrated not near the hypocenter but rather to the southeast of Gold Hill. However, it was not possible to discriminate between seismic slip and postseismic deformation occurring in the weeks to months after the mainshock, during which time a pronounced postseismic creep signal was observed at the surface (Smith and Wyss, 1968).

Segall and Du (1993) used triangulation and trilateration data to compare the slip distributions of the 1934 and 1966 earthquakes, both of which initiated at Middle Mountain and ruptured southeast. They showed that while the geodetic data for the 1966 event require slip to the southeast of a bend in the fault near Gold Hill (Fig. 1), the data for the 1934 event do not permit slip through the bend.

Using the average rates of line-length change measured on the trilateration network between 1966 and 1984, Harris and Segall (1987) estimated the interseismic slip-rate distribution along the San Andreas near Parkfield. They imaged an area of low slip rate coinciding with the inferred rupture area of the 1966 earthquake. Murray *et al.* (2001) obtained a similar result through inversion of Global Positioning System (GPS) data collected between 1991 and 1998.

Segall and Harris (1987) concluded, through assessment of a range of models for slip in the 1966 earthquake and aseismic slip during the subsequent interseismic period, that the interseismic slip deficit should have balanced the 1966 slip by 1995 at the latest. Using different methodology and additional data, Murray and Segall (2002) showed that the fault should have recovered the strain released in the 1966 earthquake by 1987 at 95% confidence and that therefore the time-predictable recurrence model (Shimazaki and Nakata, 1980) does not accurately describe earthquake recurrence at Parkfield.

In the mid 1980s, a two-color laser electronic distance measuring (EDM) network (Figs. 1, 2b) was installed at Parkfield (Langbein *et al.*, 1990). Line-length measurements were made 2–3 times per week through the 1990s, providing temporally dense observations not otherwise available in the precontinuous GPS era. In the mid-1990s a rate change was observed on several of the lines, and a number of studies used these data to infer a transient increase in aseismic slip rate lasting 2–4 years along the San Andreas in the vicinity of Middle Mountain (Gwyther *et al.*, 1996; Langbein *et al.*, 1999; Gao *et al.*, 2000; Murray and Segall, 2005).

These analyses provide a picture of crustal deformation at Parkfield at specific times. However, the limited data from the 1934 to 1966 period prevented assessment of strain accumulation and release over a complete earthquake cycle. With the occurrence of the 2004 event it is now possible to perform a comprehensive analysis of geodetic observations through a full earthquake cycle. We have undertaken such an analysis, using a variety of observations (Table 1) for the

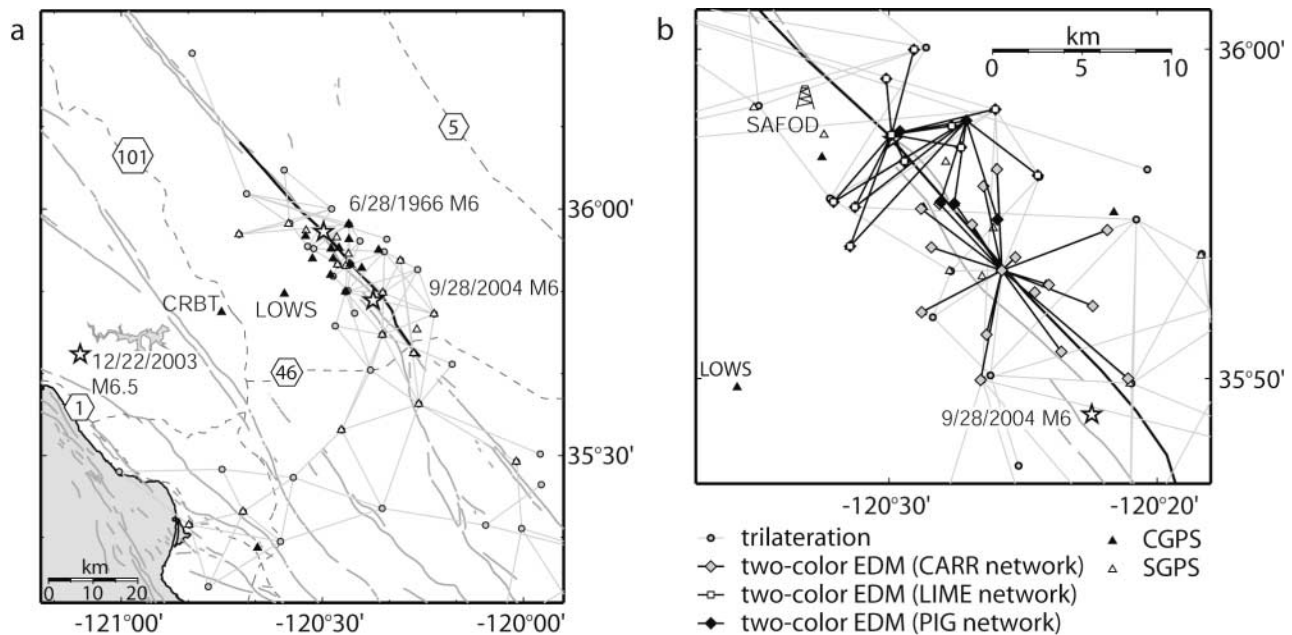


Figure 2. Geodetic networks near Parkfield, California, with data spanning the interseismic period. (a) Parkfield region; the stars mark the epicenters of the 1966 (northwestmost) and 2004 Parkfield earthquakes, as well as the 2003 San Simeon event. The heavy dark line marks the surface trace of the model fault used in the inversions for interseismic slip rate. Major highways are shown by the dashed lines labeled with their route numbers. (b) Close-up of the Parkfield area.

Table 1

Deformation Events, Defined as Earthquakes with Coseismic and Postseismic Periods or Interseismic Deformation, Spanned by Each Data Type

Data Type	Deformation Event
Triangulation	1934 coseismic and postseismic
Trilateration	1966 coseismic and postseismic 1966–1991 interseismic
Two-color EDM	1984–2004 interseismic 2004 coseismic/postseismic
SGPS	1992–2003 interseismic 2004 coseismic/postseismic
CGPS	1999–2004 interseismic 2004 coseismic 2004 postseismic

For the coseismic and postseismic periods, the specified years (1934, 1966, and 2004) refer to the year of the earthquake and not the duration of the postseismic period.

three most recent earthquakes (1934, 1996, and 2004) as well as the 1966–2004 interseismic period. We include previously unpublished line-length data from two portable two-color EDM networks at Parkfield and investigate the model resolution and uncertainties on the estimated quantities.

We use the results of this analysis to address several questions, including: (1) How does the magnitude and spa-

tial distribution of slip in 2004 compare to that in the 1934 and 1966 earthquakes, and what are the implications for the existence of characteristic earthquakes (e.g., earthquakes with the same magnitude, mechanism, and rupture segment) as described by Schwartz and Coppersmith (1984)? (2) Is there an identifiable correlation between the spatial distribution of fault slip and the distribution of microseismicity? Can seismicity locations complement geodetic data to refine our image of the fault geometry and fault slip? (3) What contribution does aseismic deformation (both interseismic creep and postseismic slip) make to the strain budget of the fault? Does a slip deficit remain that could be released in a larger earthquake southeast of Parkfield? (4) Are estimates of interseismic slip rate and slip associated with the 2004 earthquake consistent with the slip-predictable model of earthquake recurrence (Shimazaki and Nakata, 1980)?

## Data

### Triangulation Observations of the 1934 Earthquake

For the purposes of comparison to the results of our analysis for the 1966 and 2004 earthquakes, we repeat the inversion of triangulation data presented by Segall and Du (1993) to estimate the slip distribution of the 1934 earthquake. The primary data used consist of triangulation measurements made on a regional network surveyed in 1932 and 1951. We also include observations made in 1923 and 1948



on a network spanning a larger area (Fig. 1). For each of the two pairs of surveys (1923 and 1948, 1932 and 1951) we extract measurements made for the same angle before and after the earthquake and use them to calculate the angle change that occurred between surveys. We obtain 9 angle change measurements from the 1923–1948 survey pair and 149 angle changes for the 1932–1951 pair. The standard error for the angle measurements is obtained by calculating the residuals from an unweighted network adjustment as described by Yu and Segall (1996). The error estimates obtained in this manner range from 0.8 to 1.6 arc sec, and the median error for angle change measurements is 1.9 arc sec, on the order of or slightly larger than the expected signal due to the earthquake. Since the original data were direction measurements, the covariance matrix is constructed as described by Prescott (1976).

The angle changes have been corrected for the interseismic strain accumulation between surveys using the model for long-term average interseismic fault slip rate presented in this article. However, because of the large elapsed time between surveys, the data necessarily contain any postseismic signal that was present following the 1934 event. The triangulation network crosses the San Andreas southeast of the bend in the fault near Gold Hill, but few of its angles span the fault farther northwest. Therefore the resolving power of these data for slip along the central and northwestern portion of the model fault is limited.

#### Trilateration Observations of the 1966 Earthquake

Surveys of subsets of the trilateration network shown in Figure 2 were made every year between 1959 and 1991. Sixteen baselines have observations preceding the 1966 earthquake (Fig. 1). Following King *et al.* (1987), we used the trilateration time series to estimate constant rates of line-length change for each line as well as two changes in line length (offsets). The first offset accounts for coseismic displacement during the 1966 **M** 6.0 earthquake for lines that have data spanning that event. The second offset is required because the data were collected by three different agencies using varying instruments and measurement protocols. The California Department of Water Resources (CDWR) made observations between 1959 and 1969, the California Division of Mines and Geology (CDMG) did so from 1970 to 1980, and the United States Geological Survey (USGS) continued the surveying until 1991. As discussed by King *et al.* (1987), there is a systematic discrepancy between the line-length measurements made by the CDWR and those of the CDMG and USGS, with the former being consistently shorter. Therefore, an offset is estimated between the CDWR and CDMG observations. We used the nominal observation errors from the analysis of King *et al.* (1987) to weight the data collected by the different agencies in a least-squares inversion for rate of line-length change and offsets in the time series.

#### Two-Color EDM Observations of the Interseismic Period

The Parkfield permanent two-color EDM data are recorded on a radial network. A laser EDM at the center (Carr Hill) is used to measure the distance to retroreflectors located at the end of each line (Langbein *et al.*, 1987, 1990). The lines range in length from 1 to 9 km. The two-color laser modulates signals on both red and blue optical carrier frequencies to mitigate the effects of atmospheric dispersion. Observations have been made on this network since 1984. For much of this time, data were collected 2–3 times a week. Since 1999 the frequency of measurements has decreased to approximately once every 6 months as the two-color sites are replaced by continuous GPS. The rates of line-length change for this network are used in the estimation of the interseismic slip-rate distribution.

Given the large number of observations in each two-color time series, estimating rates using a simple least-squares fit to the data and propagation of errors would result in very low standard error estimates on the rates. However, the displacements of the reflector monuments used for these observations are known to exhibit random walk noise due to monument instabilities. On average the standard deviation of the random walk is  $\sim 1.3 \text{ mm/yr}^{1/2}$ , although some lines are much less stable (Langbein and Johnson, 1997; Langbein, 2004). There are also obvious annual signals in the data likely due to seasonal variations in soil moisture.

In order to obtain more realistic estimates for the rates of line-length change and their standard errors, we used the method described by Langbein (2004). In this approach the maximum likelihood method is used to simultaneously optimize the data covariance matrix and the model parameters. The covariance matrix is constructed based on an assumed error model which may include white and power law noise. Random walk and flicker noise, both of which are observed in geodetic time series, are examples of power-law noise for which the spectral index is 2 and 1 respectively. If there are sufficient observations, the amplitude of the noise components and even the spectral index for power-law noise can be reliably estimated. When fewer data are available these values can be fixed based on analyses of representative networks.

For the permanent two-color data the error model is a sum of white noise and random walk. The amplitudes of both noise sources are optimized. The model parameters include the secular rate and the amplitude of an annual sinusoidal signal. To account for the observed transient signal in the two-color data, a rate change is estimated for the time period April 1993 to July 1996, the duration of accelerated slip rate inferred by Murray and Segall (2005). The most recent survey of the permanent two-color network prior to the Parkfield 2004 earthquake was in May 2003, and the most recent portable network survey was in 2001. Therefore, contamination of the observations by the **M** 6.5 San Simeon earthquake, which occurred 60 km southwest of Parkfield on

22 December 2003 (Hardebeck *et al.*, 2004), is not a concern.

In addition to the permanent two-color network, two other networks (LIME and PIG) were surveyed using a portable two-color EDM one to two times per year between 1986 and the end of 2003 (Fig. 2b). Rates of line-length change and a rate change during the transient period were estimated for these networks, using the method described previously. However, due to the relatively small number of measurements in these time series, no annual amplitude was estimated and the amplitude of the random walk noise was fixed to  $2 \text{ mm/yr}^{1/2}$ .

#### GPS Observations of the Interseismic Period

Survey-mode GPS (SGPS) observations were made every 1 to 5 years between 1992 and 2003 on a network of benchmarks in the Parkfield area (Fig. 2). In 1999 four continuous GPS (CGPS) receivers were installed at Parkfield, augmenting two existing CGPS stations (installed in 1992 and 1996). In 2001 nine more CGPS instruments were added to the network. The survey-mode and continuous GPS data were processed with GIPSY-OASIS II software using a bias-fixed, precise point positioning technique (Zumberge *et al.*, 1997). We used nonfiducial satellite orbits and clock corrections produced by NASA's Jet Propulsion Laboratory (JPL). Included in each daily solution are 25–30 global CGPS sites that are used to estimate the seven parameters of a Helmert transformation to put the position solution in the ITRF 2000 reference frame (Boucher *et al.*, 2004).

Using SGPS data, the secular rate and a rate change between April 1993 and July 1996 were estimated for 28 benchmarks in the Parkfield area using the method of Langbein (2004) as described for the two-color data. The error model was a combination of white, random walk, and flicker noise. These measurements were made less frequently than the portable two-color observations. Therefore, the white noise amplitude for the horizontal components was fixed to 2 mm, the random walk was fixed to  $2 \text{ mm/yr}^{1/2}$ , and the flicker to  $1 \text{ mm/yr}^{1/4}$  based on observations from other GPS networks (Langbein, 2004). For the vertical component these error amplitudes were increased by a factor of 3. No annual sinusoidal amplitude was estimated.

The secular velocities of the CGPS sites were estimated for the time period following the transient deformation event. Several outliers and a common mode signal are evident in the time series for these stations. To remove the outliers and minimize the common mode we fit and removed a constant rate to the data, stacked the residual time series, removed the average daily residuals, and added back the secular trend. We then estimated velocities for these sites using data up to the time of the San Simeon earthquake, again employing the approach of Langbein (2004). The error model is a sum of white, random walk, and flicker noise. The white and flicker noise amplitudes were estimated, and the random walk amplitude was fixed to  $1 \text{ mm/yr}^{1/2}$ .

#### GPS Observations of the 2004 Earthquake

Fourteen CGPS instruments (Fig. 1), operating at a 1-Hz sampling rate (Langbein and Bock, 2004), recorded data during the 2004 M 6. Parkfield earthquake. Until recently, CGPS measurements have generally been used to estimate a coseismic offset as the difference between the daily average position on the day prior to the earthquake and that on the day following the event. In this case, it is not possible to separate the true coseismic signal from postseismic displacement that began immediately following the earthquake. The high sampling rate for the Parkfield continuous stations enables subdaily position estimates, and thus permits estimation of coseismic offsets over a time span of minutes rather than hours. In addition to the CGPS data, 13 SGPS receivers were deployed in the days after the earthquake (Fig. 1), and data were collected for this subset of the Parkfield survey-mode network throughout the first two months of the postseismic period. A larger subset of the Parkfield SGPS network was resurveyed in April 2005.

The processing of the GPS data for the 2004 earthquake and the estimation of coseismic and postseismic displacements is described in detail in Langbein *et al.* (2006). The postseismic data were fit with an Omori Law to capture the relaxation of the postseismic slip with time, and four quantities were estimated: the coseismic displacement, the coseismic displacement plus that during the first 60 days of the postseismic period, the coseismic displacement plus that during the first 230 days of the postseismic period (up to April 2005), and the displacement between days 60 and 230 of the postseismic period. The CGPS data for the first 100 sec after the earthquake were not used to avoid the complication of passing seismic waves. Therefore, the coseismic displacement estimates actually include any displacement in the first 2 min following the earthquake. For the campaign data it was not possible to separate the coseismic from postseismic offsets, so for these stations no coseismic offsets were estimated.

For the continuous data, the estimated coseismic offsets are about 75% the size of those found using daily solutions (Langbein *et al.*, 2006). This is evidence for a significant amount of postseismic slip beginning immediately after the earthquake. An important feature of the CGPS coseismic displacements (Fig. 3a) is that the station at Carr Hill moved to the southeast coseismically, contrary to what would be expected given its location to the west of the mapped surface trace of the fault. During the first 60 days of the postseismic period its displacement reversed, producing a net displacement to the northwest.

#### Two-Color EDM Observations of the 2004 Earthquake Postseismic Period

Observations were made on the permanent two-color EDM network 60 days and 230 days following the 2004 Parkfield earthquake. With the exception of line CARR-GOLD, these data were used to estimate line-length changes

due to coseismic slip plus the first 60 days of the postseismic period, and the line-length changes between days 60 and 230 of the postseismic period. For line CARR-GOLD the available observations only permitted estimation of the line-length change due to coseismic slip plus the first 230 days of the postseismic period.

### Method

In order to assess the distribution of cumulative slip along the San Andreas fault at Parkfield, we inverted geodetic data for the spatial distribution of slip or slip rate over different time intervals. Here we describe the details of our approach.

#### Fault Geometry

The inversion of geodetic data for fault slip requires an assumed fault geometry. The approach often taken is to approximate the fault plane by a large rectangular dislocation aligned with the mapped strike, whose size is defined by information such as the extent of aftershocks or inferred fault segment boundaries. This fault plane is divided into a grid of smaller rectangular dislocations (subfaults). The Green's functions relating slip on the dislocations to surface displacement are calculated, assuming a homogeneous elastic half-space, for example, following Okada (1985). Since the displacements are linearly related to slip on the subfaults, the data may be inverted for the slip distribution using traditional inversion techniques. Although assuming a planar fault is clearly an approximation, in many cases the geodetic stations are sufficiently far from the fault that they are insensitive to finer scale features of the fault geometry.

The mapped surface trace of the San Andreas near Parkfield is actively creeping during the interseismic period and is readily identifiable. Therefore, past Parkfield studies have assumed a simple fault geometry consisting of a planar vertical strike-slip fault. However, the displacement of the CGPS station at Carr Hill (CARH) during and after the 2004 earthquake was anomalous. Although located 0.5 km west of the

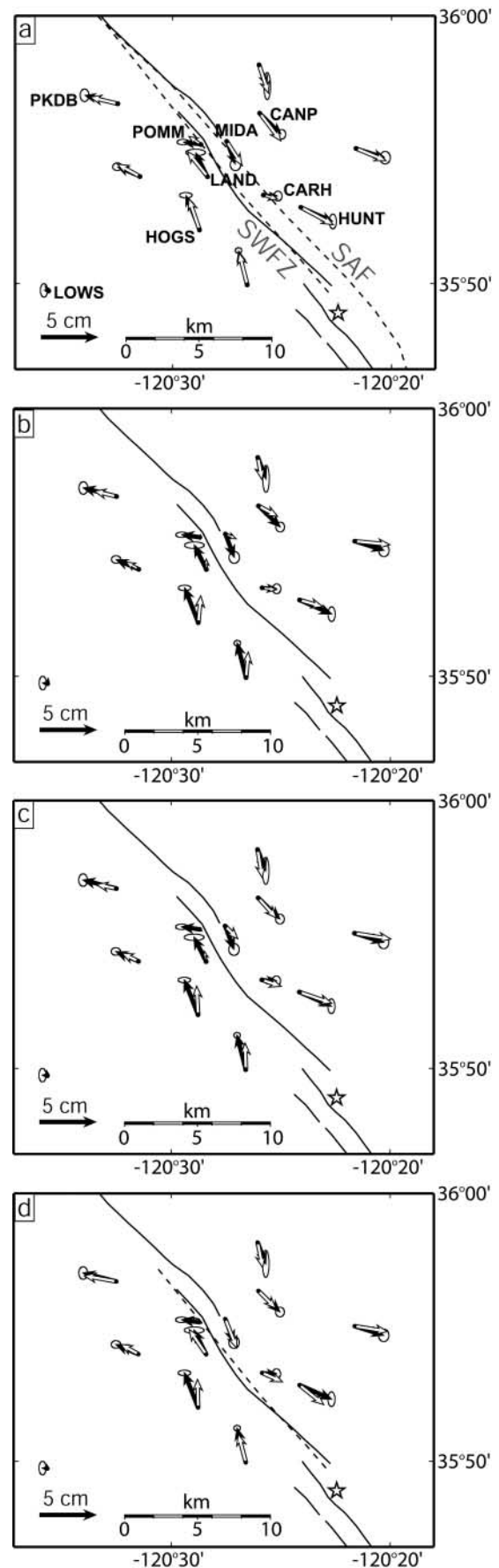
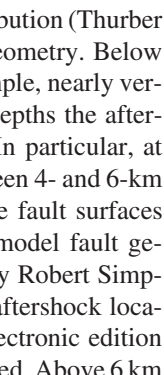


Figure 3. Observed (black with 95% confidence ellipses) coseismic GPS data for the 2004 earthquake (epicenter indicated by star) relative to CRBT (see Fig. 2 for location) and predicted (white) displacements from modeling using the different subsets of subfaults shown in Figure 9. See text for details regarding choice of subfaults used. Solid black lines are mapped surface traces of the San Andreas and subsidiary faults in the Parkfield area. (a) Fit to the data using the full fault geometry (all subfaults). Black dashed lines are the surface traces of the primary model fault surface (northeastern trace labeled SAF) and the SWFZ surface. (b–d) Fit to the data using the subsets of subfaults shown in Figure 9b–d, respectively. (d) Dashed black line is intersection of model fault with the Earth's surface.



mapped creeping trace, coseismically CARH moved south-east, as if it were east of the fault. This implies that coseismic slip occurred on a fault surface to the southwest of the actively creeping San Andreas.

Fault traces subparallel to the creeping SAF trace have in fact been mapped to the southwest. The most well-known is the Southwest Fracture Zone (SWFZ), located along the central portion of the Parkfield segment near Carr Hill (Fig. 3a). It exhibited ground cracking following both the 1966 and 2004 earthquakes (Brown *et al.*, 1967; Langbein *et al.*, 2005; Rymer *et al.*, 2006). Observations from creepmeters, the two-color laser, and survey-mode GPS during the interseismic period have suggested that an approximately 2-km-wide zone of distributed deformation exists to the west of the mapped fault trace in the vicinity of Middle Mountain (Langbein *et al.*, 1990; Roeloffs, 2001). Mapped fault traces southwest of the main trace in that area may connect to the SWFZ farther southeast (Rymer *et al.*, 2006). Carr Hill is situated between the mapped main trace and the SWFZ. The coseismic displacement at this location cannot be fit using a simple fault model aligned with the mapped main trace of the San Andreas. Primarily for this reason, and also because there are a number of other geodetic monuments located near the fault trace, we decided to consider a more complex fault geometry than the single planar fault that was used in initial analyses (e.g., Bakun *et al.*, 2005; Langbein *et al.*, 2005) of geodetic data for the 2004 Parkfield earthquake.

The precisely relocated aftershock distribution (Thurber *et al.*, 2006) provides a guide to the fault geometry. Below  $\sim 6$  km, the aftershocks delineate a fairly simple, nearly vertical, fault surface. However, at shallower depths the aftershocks suggest a more complex structure. In particular, at several points along strike, aftershocks between 4- and 6-km depth appear to define two branching active fault surfaces (e.g., figure 2 of Bakun *et al.*, [2005]). A model fault geometry for the inversions was constructed by Robert Simpson (USGS) by fitting surfaces through the aftershock locations (Fig. 4,  Fig. S1, available in the electronic edition of BSSA). Below 6 km a single surface sufficed. Above 6 km one surface branched toward the northeast to connect with the main creeping SAF trace, and a second branched in a more nearly vertical direction to reach the surface along a line that included the mapped SWFZ trace. The primary fault used in our modeling consists of the first branch (which joins the main SAF trace) plus the deeper section from 6 to 14 km. This fault surface is 81 km long, and its midpoint is at  $35.86^\circ$  N,  $-120.41^\circ$  E. A secondary fault used in the modeling consisted of the part of the second branch from  $\sim 15$  km northwest to  $\sim 9$  km southeast of Carr Hill, extending from 6-km depth up to the SWFZ surface trace.

Both fault surfaces are nonplanar and therefore are divided into triangular dislocations. The Green's functions for slip on triangular dislocations were calculated using a subroutine written by W. Stuart (USGS) based on work by Comninou and Dundurs (1975). Each triangle's along-strike dimension is approximately 3 km. The down-dip dimension

of the triangles varies from 100 to 2 km. The shallowest row of subfaults has a down-dip width of 100 m. The second row is 750 m wide, the third row is 1.5 km, and the subsequent rows (from a depth of 2 km to 14 km) are 2 km wide. The average dip of the primary fault surface above 6-km depth between Middle Mountain and Gold Hill is  $\sim 83^\circ$  southwest, and outside of this reach (i.e., to the northwest and southeast) the average dip is  $\sim 85^\circ$  to the northeast. The average dip of the entire primary fault below 6 km is  $\sim 89^\circ$  to the northeast. The average dip of the secondary fault surface is  $\sim 86^\circ$  northeast.

The secondary fault is necessary to fit the coseismic CGPS observations at Carr Hill in the 2004 earthquake and is supported by the pattern of aftershocks, surface creep in the early postseismic period (Langbein *et al.*, 2006; Lienkaemper *et al.*, 2006; Rymer *et al.*, 2006) and InSAR observations (E. Fielding, personal comm. 2006). To facilitate comparison of slip estimates made for different time periods, the nonplanar primary fault surface is used as the model geometry for all inversions. The secondary fault surface is included in the fault geometry for the inversion of data for the 2004 coseismic and postseismic periods only.

#### Model Regularization

We assume that slip along the San Andreas will be purely strike slip and require the slip to be right lateral by applying a nonnegativity constraint. To regularize the inversion, we apply spatial smoothing using the finite-difference approximation of the Laplacian operator ( $\nabla^2$ ). For triangular subfaults we construct a smoothing operator as discussed in Maerten *et al.* (2005) and Desbrun *et al.* (1999). For models in which both the main and southwest fault surfaces are used, the smoothing is applied to each surface separately. The relative weight put on smoothing versus fitting the data is controlled by a smoothing parameter,  $\gamma$ , which is chosen using cross validation (CV) (Wahba, 1990). In CV, for a given value of  $\gamma$ , the inversion is repeated, each time leaving out one station's data. The resulting slip distribution at each iteration is used to predict the omitted data. The squared residuals between omitted and predicted data, summed over all stations, is the cross validation sum of squares (CVSS) for that  $\gamma$ . If  $\gamma$  is too high, the solution will be rough and tend to model noise, preventing it from adequately predicting the omitted datum. Solutions with too much smoothing (lower  $\gamma$ ) will have greater misfit. The value of  $\gamma$  with the smallest CVSS is optimal.

With the inclusion of spatial smoothing, the system of equations to solve is

$$\begin{bmatrix} \mathbf{d} \\ 0 \end{bmatrix} = \begin{bmatrix} \mathbf{G} \\ \nabla^2 \end{bmatrix} \mathbf{s} + \boldsymbol{\varepsilon} \quad \boldsymbol{\varepsilon} \sim N(0, \boldsymbol{\Sigma}) \quad (1)$$

$$\boldsymbol{\Sigma} = \begin{bmatrix} \boldsymbol{\Sigma}_d & 0 \\ 0 & \gamma^2 \mathbf{I} \end{bmatrix}, \quad (2)$$

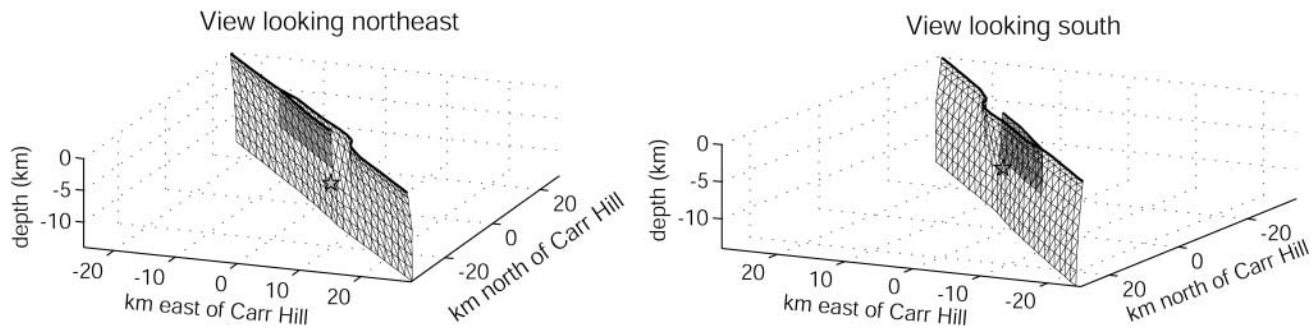


Figure 4. Model fault geometry looking from two angles. Gray shaded portion is the subsidiary fault surface that intersects the mapped SWFZ at the Earth's surface. Star is hypocenter of the Parkfield 2004  $M$  6.0 earthquake.

where  $\mathbf{d}$  is the data vector,  $\mathbf{G}$  is the matrix of dislocation Green's functions relating fault slip to displacement and/or line-length change,  $\mathbf{s}$  is the vector of slip estimates, and the errors,  $\varepsilon$ , are assumed to be normally distributed with zero mean and covariance  $\Sigma$ . The covariance matrix,  $\Sigma$ , is comprised of the data covariance ( $\Sigma_d$ ) and the weighting (controlled by  $\gamma$ ) for the smoothing constraints, where  $\mathbf{I}$  is the identity matrix.

#### Inversions for Slip over Specific Time Intervals

**1934 Earthquake.** Using the angle change data, we estimate the distribution of slip in the 1934 earthquake using the primary fault model described previously to enable direct comparison of the 1934 slip with the estimates we obtain for the 1966 and 2004 events. Although these data have been corrected for interseismic deformation, because of the large elapsed time between surveys, the data contain any postseismic signal that was present following this event.

Lienkaemper and Prescott (1989) used offset cultural features to estimate that the surface slip for the 1934 and 1966 Parkfield events was about 30 cm at the Parkfield bridge, in the central portion of the ruptured segment, and tapered to about 15 cm within 15–20 km along strike in either direction. Based on these estimates, we used  $30 \pm 20$  cm as a weak constraint on the slip estimates for the upper two rows of subfaults (the upper 850 m) of the model fault surface from 10 km northwest to 15 km southeast of Carr Hill. This was achieved by a one-to-one mapping between the peak offset of 30 cm inferred by Lienkaemper and Prescott (1989) and the slip estimates for the subfaults that coincided with the along-strike extent of the surface offsets. These weak constraints were assigned a standard error of 20 cm.

**1966 Earthquake.** The slip in the 1966 earthquake was inferred using estimates of line-length change for the trilateration lines shown in Figure 1. The earthquake occurred on 27 June 1966 (local time), and the majority of these lines were resurveyed between 6 July and 28 July. A strong postseismic surface creep signal was recorded following this

earthquake (Smith and Wyss, 1968), but coseismic and postseismic slip cannot be differentiated given the timing of the trilateration surveys.

In the inversions of trilateration data for slip in the 1966 earthquake, we apply bounds derived from the postseismic surface creep observed by Smith and Wyss (1968) to the slip estimates for elements in the upper 850 m of our fault model. The observed creep extended from approximately 15 km southeast of Carr Hill to 25 km northwest of Carr Hill (Smith and Wyss, 1968). Smith and Wyss (1968) traced the temporal progression of the creep at eight locations along strike from directly after the earthquake until the summer of 1967. Their measurement dates of 7 July and 15 August, 1966 most closely coincide with the time spanned by the trilateration surveys. To be consistent with the timing of postseismic trilateration measurements, we estimate the surface creep up until 28 July 1966 from figure 4 of Smith and Wyss (1968) and use the 7 July observations and the 28 July estimates to define bounds on the surface offset that had occurred at the time of the trilateration survey. In other words, we assume that at the time of the trilateration measurements at least as much surface creep as was observed on 7 July and possibly as much as that estimated for 28 July had occurred. We used linear interpolation of the observations presented in figure 10 of Smith and Wyss (1968) to fill along-strike gaps in coverage. To allow for uncertainty in the surface offset estimates, for subfaults that coincide with surface creep measurement locations we use a lower bound that is 3 mm less than the observed 7 July offset and an upper bound 3 mm greater than the estimated 28 July offset. For subfaults located between measurement locations, the lower bound is 10 mm less than the 7 July offset interpolated at that point along strike, and the upper bound is 10 mm more than the interpolated 28 July offset.

**Interseismic Period, 1966–2004.** Previous studies (e.g., Harris and Segall, 1987; Murray *et al.*, 2001) have shown that interseismic deformation at Parkfield is dominated by low slip rate over much of the fault and the transition from locked to creeping behavior to the northwest of Parkfield. However, evidence exists for a transient slip-rate increase



during the mid-1990s (Murray and Segall, [2005] and references therein). It is not possible to know whether other similar transient slip events have occurred at Parkfield prior to the installation of the two-color EDM network in 1984. Therefore, we assume that Parkfield can be characterized by a constant secular slip-rate distribution throughout the interseismic period, modulated by the one transient event for which we have data.

Although some geodetic observations for the interseismic period have shown evidence for distributed deformation west of Middle Mountain (Langbein *et al.*, 1990), including the secondary (southwest) fault surface in the interseismic model did not improve the fit to these data. Furthermore, the two creepmeters on the SWFZ did not record any significant creep during the interseismic period (Roeloffs, 2001). Therefore, to minimize the number of model parameters to be estimated, we did not include the secondary fault in the interseismic inversions.

In the inversions for interseismic slip-rate distribution, to simulate the effect of the adjacent creeping and locked segments of the San Andreas to the northwest and southeast, respectively, of the Parkfield segment, we appended a vertical rectangular dislocation 100 km in along-strike length and 14 km wide on either end of the primary fault surface. A vertical rectangular dislocation 1000 km long and wide was centered below the primary fault to represent deep slip and far-field plate motion (Savage, 1990). The strike of these three large dislocations was set to the average strike of the primary fault surface (approximately N40°W).

We estimate the secular slip-rate distribution during the interseismic period through joint inversion of the average rates of line-length change for the trilateration and two-color EDM networks and the average velocities for the SGPS and CGPS sites. Rather than reference the GPS data to a specific station, we include a three-component translation of the network as an estimated quantity. We also estimate a two-component translation of the central monument of each two-color network. The temporal coverage of the data types varies, as older measurement methods have been replaced by newer technology. No single data type spans the entire interseismic period. To address the period of transient deformation, we use the rate-change estimates for the two-color EDM networks to estimate the spatial distribution of slip-rate change for the period April 1993 to July 1996. We do not require the estimated quantity to be positive. Negative values indicate a slowing down of the interseismic slip rate.

Surface creep rates in the Parkfield region have been estimated using data from creepmeters, small aperture networks, and alignment arrays (Burford and Harsh, 1980; Lisowski and Prescott, 1981, Harris and Segall, 1987) as well as recent GPS observations for the creeping section of the San Andreas fault (Titus *et al.*, 2005). We applied these creep rates as constraints on the slip-rate estimates for sub-faults in the upper 100 m of the fault surface in the same manner as for the 1934 earthquake. The creep-rate constraints range from 27 mm/yr at the northwest end of the

subdivided fault surface to 1 mm/yr at the southeast end. For the central 45 km of the fault, the constraints were assigned uncertainties of 1.5 mm/yr. To the northwest and southeast, where there are fewer measurements, the uncertainties are 2 mm/yr. In a similar way, the large dislocation representing the creeping section was constrained to  $27 \pm 1.5$  mm/yr and the locked section to  $1 \pm 1$  mm/yr. The large dislocation representing slip below the transition depth was constrained to  $33 \pm 1$  mm/yr based on the results of Murray *et al.* (2001). We do not include the creeping, locked, or deep blocks in the inversion for the distribution of transient slip-rate change, nor do we apply any surface constraints.

*2004 Coseismic and Postseismic Period.* The coseismic and postseismic data (GPS and two-color) correspond to four time periods: (1) coseismic, (2) coseismic plus the first 60 days of the postseismic period, (3) coseismic plus 230 days, and (4) days 60–230 of the postseismic period. These data were inverted to simultaneously estimate the coseismic slip, the slip during the first 60 days of the postseismic period, and the slip between days 60 and 230 as follows:

$$\begin{bmatrix} \mathbf{d}_c \\ \mathbf{d}_{c+60} \\ \mathbf{d}_{c+230} \\ \mathbf{d}_{60-230} \end{bmatrix} = \begin{bmatrix} \mathbf{G}_c & 0 & 0 \\ \mathbf{G}_c & \mathbf{G}_{60} & 0 \\ \mathbf{G}_c & \mathbf{G}_{60} & \mathbf{G}_{60-230} \\ 0 & 0 & \mathbf{G}_{60-230} \end{bmatrix} \begin{bmatrix} \mathbf{s}_c \\ \mathbf{s}_{60} \\ \mathbf{s}_{60-230} \end{bmatrix}, \quad (3)$$

where  $\mathbf{d}$  are data,  $\mathbf{G}$  are Green's functions, and  $\mathbf{s}$  are slip estimates. The subscripts are as follows:  $c$  is coseismic,  $c+60$  is coseismic plus the first 60 days of the postseismic period,  $c+230$  is coseismic plus the first 230 days, and  $60-230$  indicates days 60 to 230 of the postseismic. The simultaneous inversion ensures that the contribution from slip at each time period to the displacement signal is consistent. Spatial smoothing is applied as shown in equations (1) and (2).

Essentially no coseismic slip was observed at the surface except at the northwest end of the SWFZ (Langbein *et al.*, 2006). Within 0.5–3 hr after the mainshock, creepmeters began showing some surface offset (Langbein *et al.*, 2006). Creep continued along the main San Andreas trace throughout the postseismic period covered by the geodetic data. After the initial offset on the SWFZ, creepmeters (Langbein *et al.*, 2006) and measurements of nail quadrilaterals (Rymer *et al.*, 2006) showed no further movement, while alignment array data indicate that up to  $\sim 1.6$  cm of surface creep was observed there during the first 6 months following the mainshock (Lienkaemper *et al.*, 2006). The surface offsets and uncertainties estimated by Lienkaemper *et al.* (2006) using alignment array data for 60 and 230 days following the earthquake are used as constraints on the upper 100 m of the primary fault surface. This is achieved in the same way as was done for the interseismic period. The coseismic slip on the upper 100 m is constrained to 0 with an uncertainty of 5 mm.

### Model Resolution

In order to assess the extent to which features of the estimated slip distributions are well resolved, we calculate the model resolution matrix ( $\mathbf{R}$ ) for each inversion. Due to the use of nonnegativity constraints and bounds on model parameters, the inverse problem is nonlinear. Therefore, we follow the approach outlined by Du *et al.* (1993). For each dislocation in our model we perform a forward calculation to obtain synthetic data due to unit slip on the dislocation. We then invert the synthetic data, using the same smoothing parameter,  $\gamma$ , as with the observed data, to obtain an estimate of the input slip distribution, which is one column of  $\mathbf{R}$ . We repeat this for each subfault to construct the complete resolution matrix. If all model parameters were perfectly resolved,  $\mathbf{R}$  would be the identity matrix. The diagonal terms of  $\mathbf{R}$  quantify the amplitude resolution, and each column shows the spatial resolution as indicated by smearing of the true slip or slip artifacts imaged far from the actual source.

### Uncertainties

One goal of this study is to quantify the spatial distribution of slip deficit along the fault through a complete earthquake cycle with an estimate of the uncertainties on the inferred slip deficit. For linear inverse problems the model covariance is easily computed. However, due to the nonlinearity of the inversion we use the bootstrap (Efron and Tibshirani, 1993) instead. The bootstrap is a statistical technique in which the inversion is repeated a large number of times, each time using a dataset randomly sampled with replacement from the original data. Because the data are sampled with replacement, each sampled dataset has the same number of observations as the original, although some may be repeated and others may not appear at all. Confidence intervals on the model parameters can be obtained from the resulting distribution of solutions. We perform a bootstrap with 2000 resamples for each of the inversions (1966 coseismic, interseismic secular rate, transient rate change, and 2004 coseismic and postseismic slip).

## Results

### 1934 Earthquake

The slip distribution for the 1934 event estimated from the triangulation data is shown in Figure 5a. The inferred slip in this event is concentrated in the central part of the fault, and little slip is imaged southeast of the bend in the fault near Gold Hill. The moment of this slip distribution is  $4.1 \times 10^{18}$  N m, which corresponds to a moment magnitude ( $M_w$ ) of 6.3. This is in good agreement with Segall and Du's (1993) moment estimate of  $4.3 \times 10^{18}$  N m, although the peak slip we estimate, 0.49 m, is somewhat lower than the  $\sim 0.65$  m found by Segall and Du. The primary difference between the two studies is that the model fault used by Segall

and Du (1993) extended only  $\sim 15$  km northwest of Carr Hill, therefore limiting the extent of slip to the northwest.

The resolution analysis indicates that, as would be expected, the resolving power is greatest at shallow depths (down to 4 km) where the triangulation arc crosses the fault around 10 km southeast of the bend in the fault. Outside of this area, the resolution drops off sharply. The resolution analysis also suggests that slip at some points southeast of the bend, although resolved primarily on the southeast portion of the fault, may be imaged to a lesser degree on the fault northwest of the bend.

The combined effect of the data's low signal-to-noise ratio and the deficiencies in network coverage limits the conclusions that can be drawn from this analysis. For instance, the amplitude and northwestward extent of the slip distribution are poorly constrained. However in systematic testing using a range of smoothing parameters, with and without surface constraints, imaged slip was always confined northwest of the bend in the fault.

### 1966 Earthquake

In contrast to the 1934 event, the slip inferred from the trilateration data for the 1966 earthquake extends well southeast of the bend in the fault near Gold Hill (Fig. 5b). The moment of this slip distribution is  $5.2 \times 10^{18}$  N m (equivalent  $M_w$  6.4), and the peak slip is 0.42 m. The peak slip

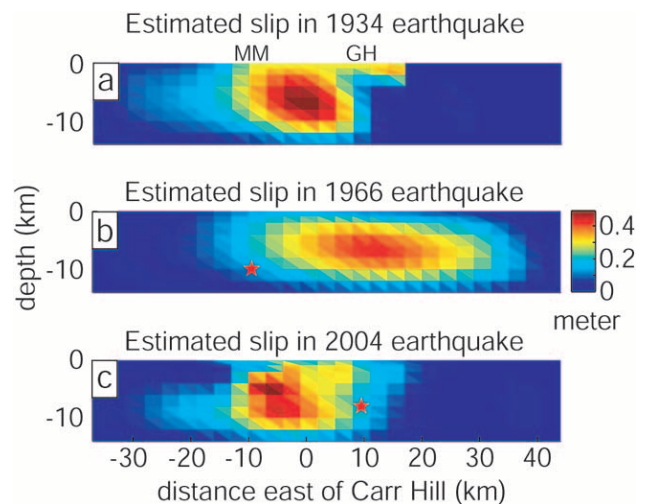


Figure 5. Slip distributions (coseismic plus postseismic) for the three most recent  $M$  6.0 earthquakes at Parkfield. The slip has been projected onto a planar representation (vertical, striking  $N40^\circ W$ ) of the nonplanar model geometry for figure clarity. Stars mark hypocenters. MM, Middle Mountain; GH, Gold Hill. Slip associated with the (a) 8 June 1934 earthquake, (b) 28 June 1966 earthquake, and (c) 28 September 2004 earthquake (coseismic plus first 230 days of postseismic). Estimated slip on the fault surface that intersects the SWFZ at the Earth's surface has been added to that for the primary fault surface.

estimate is essentially the same as that found by Segall and Du (1993), but the moment estimate is higher than their  $4.4 \times 10^{18}$  N m due to the difference in model fault length.

Due to the network configuration, the resolution is best in the vicinity of the bend in the fault. The area of poorest resolution is along the central portion of the fault between Middle Mountain and Gold Hill and over the northwestmost  $\sim 6$  km. The along-strike resolution length for the southeastern half of the fault is  $\sim 20$  km and for the northwestern half is  $\sim 30$  km. The spatial resolution in the dip direction ranges from  $\sim 8$  to 12 km. (E The observed and predicted data, residuals, and standard errors of the observations are listed in Table S1a in the electronic edition of BSSA.)

### Interseismic Period

The interseismic slip-rate distribution from the long-term average geodetic rates is shown in Figure 6a. In the vicinity of Middle Mountain the fault transitions from creeping behavior at all depths to being essentially locked below 4 km. The maximum estimated slip rate is 30 mm/yr. The fit to the GPS data is shown in Figure 7 and in (E Table S1b in the electronic edition of BSSA). The overall fit is good, with a variance reduction, defined as  $100 \times [1 - (\mathbf{r}^T \Sigma^{-1} \mathbf{r}) / (\mathbf{d}^T \Sigma^{-1} \mathbf{d})]$  where  $\mathbf{r} = \mathbf{d} - \mathbf{d}_{\text{estimated}}$ , of 99.6%. The fit to two-color data (E Table S1c in the electronic edition of BSSA) has a variance reduction of 97.9%. Four of the 37 lines are not fit at the  $2\sigma$  level. One, CARR-MIDD, probably lies in a zone of distributed deformation west of Middle Mountain (Langbein *et al.*, 1990). The other three are baselines from the PIG portable network, which may experience local ground instability. The variance reduction for the trilateration data is 95.9% with 80% of the data fit at 95% confidence (E Table S1d in the electronic edition of BSSA).

The distribution of change in slip rate between April 1993 and July 1996 estimated from the two-color EDM data is shown in Figure 6b, and the fit to the data is shown in (E Table S1e in the electronic edition of BSSA). Since the estimated quantity is slip-rate change, no nonnegativity constraint was used. A small area in which the inferred slip-rate change is negative exists on the northwestern end of the fault; however, the data have essentially no resolving power in this area. The sum of the long-term average rate and the rate change is shown in Figure 6c.

Features of the slip distribution are best resolved in the area between Middle Mountain and Carr Hill, which has long been a focus of study because the 1934 and 1966 earthquakes nucleated there. At depths of 4 km the spatial resolution is  $\sim 6$  km along strike and downdip near Middle Mountain. Elsewhere on the fault it is  $\sim 9$  km. The resolvable scale of features at 6-km depth is  $\sim 9$  km northwest of the bend in the fault and  $\sim 12$  km to the southeast. At 8-km depth the resolvable scale is  $\sim 11$  km. At 9- to 10-km depth the resolution is weak southeast of Middle Mountain, and below 11-km depth the resolving power is very low for the entire length of the fault.

### 2004 Earthquake

Figure 8a–c shows slip distributions for the 2004 coseismic slip, the first 60 days of the postseismic period, and days 60 to 230 of the postseismic inferred from GPS and two-color EDM data. Figure 8d shows the coseismic slip plus the first 230 days of the postseismic.

The coseismic slip has a peak value of 0.27 m, and the moment of this slip is  $1.3 \times 10^{18}$  N m (equivalent  $M_w$  6.0). This moment estimate is greater than the  $1.1 \times 10^{18}$  N m inferred by Langbein *et al.* (2006); however, the peak amplitude we estimate is lower. The majority of slip is concentrated between Middle Mountain and Gold Hill, with only minor slip above the hypocenter. The maximum slip on the SWFZ is 10 cm, and the average slip on this fault surface, weighted by each subfault's area, is 2 cm. The slip along the SWFZ is required to fit the data at Carr Hill, as well as that at LAND, at 95% confidence. In the vicinity of Carr Hill the fault surface as defined by seismicity at depths greater than  $\sim 6$  km lies more directly beneath the SWFZ than the main SAF trace, and therefore is west of the CARH CGPS station at these depths. However, the displacement at Carr Hill cannot be explained simply as a result of coseismic slip below 6 km on that fault surface. The data also cannot be fit at 95% confidence using a single fault surface regardless of which mapped surface trace it intersects. Due to their proximity to the mapped surface traces, stations MIDA and POMM are also sensitive to the choice of fault model; however, these stations' coseismic data are poorly fit regardless of the model geometry used. Overall, the variance reduction for the coseismic GPS data is 97% (E Table S1f in the electronic edition of BSSA).

During the first 60 days of the postseismic period, slip spread outward from the area of coseismic slip, concentrating at shallow depths and extending to the northwest. The results indicate that postseismic slip also occurred along the SWFZ. Lienkaemper *et al.* (2006) report evidence from alignment array data for continued postseismic slip along the SWFZ during the first 6 months of the postseismic period; however, their inferred maximum postseismic near-surface slip of 1.6 cm was concentrated at the south end of the SWFZ. The moment of the postseismic slip we estimated for the 60 days following the earthquake using GPS and two-color data is  $2.0 \times 10^{18}$  N m, greater than the coseismic moment release. Despite differences in the details of the distribution, the estimate presented here has the same moment as that obtained by Langbein *et al.* (2006). The variance reduction for the GPS data for the coseismic plus first 60 days of postseismic is 99.6% (E Table S1g, Fig. S2 in the electronic edition of BSSA). The two-color data are fit at 95% confidence (E Table S1h in the electronic edition of BSSA).

Over the time from 60 to 230 days after the earthquake, the fault continued to slip in the areas that experienced the greatest offset during the first 60 days of the postseismic period. Essentially no postseismic slip is imaged along the SWFZ during this time. The moment of the estimated slip



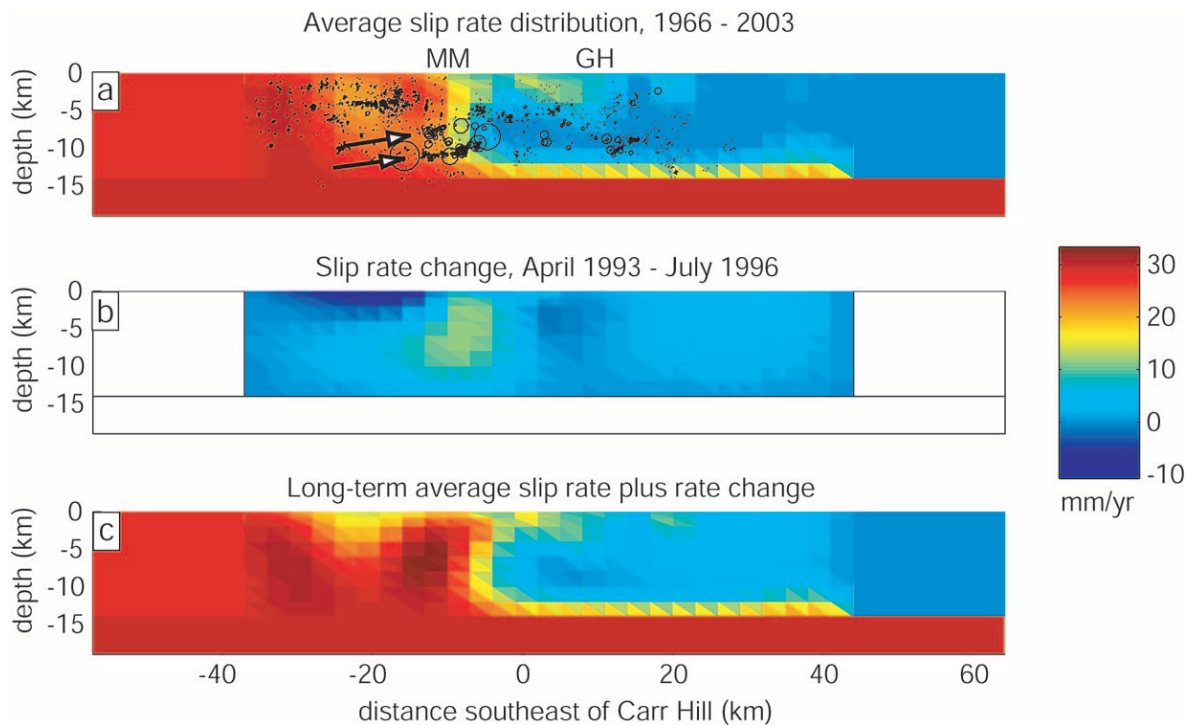


Figure 6. Interseismic slip-rate distribution. The slip rate has been projected onto a planar representation (vertical, striking N40°W) of the nonplanar model geometry for figure clarity. (a) Long-term average slip-rate distribution, 1966–2003, with interseismic background seismicity from 1 January 1970 to 27 September 2004 (Waldhauser *et al.*, 2004; Thurber *et al.*, 2006) superimposed; earthquakes are plotted as the equivalent rupture area of a 3 MPa stress-drop crack; arrows indicate location of two streaks of seismicity that bracket the 1966 nucleation zone. (b) Slip-rate change between April 1993 and July 1996 estimated from changes in rates of line-length change for the permanent and portable two-color EDM networks; positive slip-rate change indicates slip at a rate faster than the long-term average shown in Figure 6a; (c) Sum of the slip-rate distributions in the first two panels. MM, Middle Mountain; GH, Gold Hill. Large rectangular blocks surrounding the gridded fault planes represent the creeping section of the SAF northwest of Parkfield, the locked section southeast, and the deeper fault surface that slips at  $\sim 33$  mm/yr.

for this time period is  $0.6 \times 10^{18}$  N m, less than the  $0.8 \times 10^{18}$  N m inferred by Langbein *et al.* (2006). The variance reduction for the GPS data spanning the coseismic period and the following 230 days is 96.6% (Table S1i, Fig. S3 in the electronic edition of BSSA) and that for the GPS data spanning days 60 to 230 of the postseismic period is 99.3% (Table S1j, Fig. S4 in the electronic edition of BSSA). The variance reduction for two-color data in days 60–230 of the postseismic period is 99.7% (Table S1k in the electronic edition of BSSA). One line (CARR–CANN) is not fit at  $2\sigma$ .

The total slip associated with the Parkfield earthquake and the first 230 days of the postseismic period is shown in Figure 8d. It has a moment of  $3.9 \times 10^{18}$  N m, equivalent to an  $M_w$  6.3 earthquake. This moment estimate is the same as the total moment of the slip estimates of Langbein *et al.* (2006). The resolution of the slip distributions for this event is discussed in Langbein *et al.* (2006). In summary, the scale of the spatial resolution is  $\sim 10$  km on average.

## Discussion

### Spatial Relationship between Slip and Seismicity

Several studies have postulated a correlation between spatial patterns of seismicity and fault slip in which aftershocks occur at the highly stressed edges of the rupture zone, and interseismic microearthquakes occur at the boundary between creeping and locked areas of the fault (Mendoza and Hartzell, 1988; Oppenheimer *et al.*, 1990; Schaff *et al.*, 2002; Manaker *et al.*, 2003; Waldhauser *et al.*, 2004). The coseismic slip distribution of the Parkfield 2004 earthquake inferred from the continuous GPS data shows a qualitative spatial correlation with the distribution of aftershocks (Thurber *et al.*, 2006) that occurred during the first day following the earthquake (Fig. 9a). The aftershocks outline an area between  $-10$  and  $+15$  km along strike at depths of 5–10 km.

We explored whether the coseismic GPS data could be fit with a model in which slip was confined to the area sur-

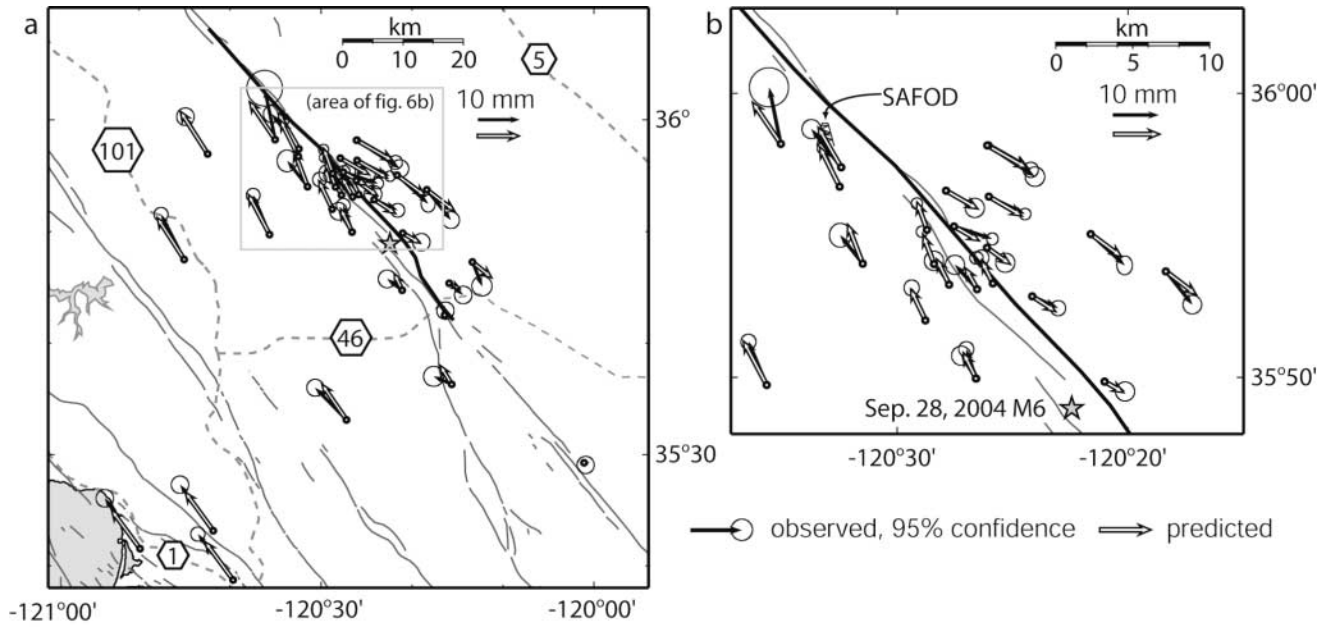


Figure 7. Observed and predicted GPS velocities for the interseismic period. Black are observed velocities with 95% confidence ellipses, and white are predicted. Star is epicenter of the 2004 earthquake. Heavy black line is surface trace of model fault plane. Solid gray lines are faults. (a) Parkfield region; dashed gray lines are major highways labeled with their route numbers; (b) close-up of central portion. SAFOD, San Andreas Fault Observatory at Depth.

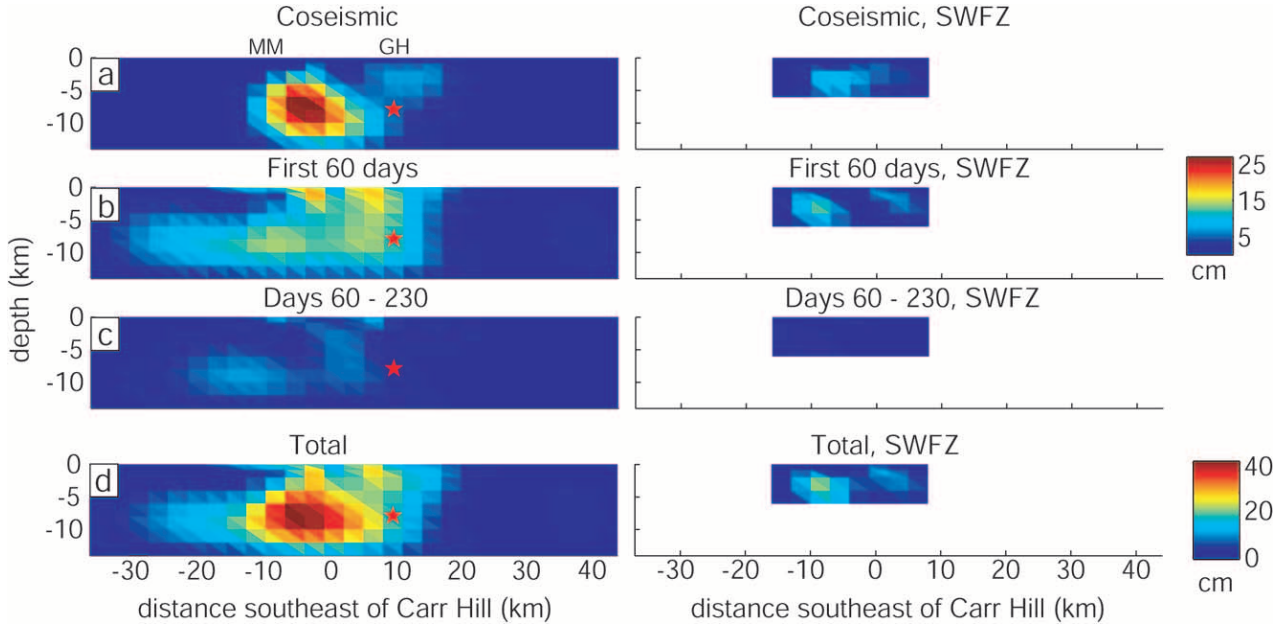


Figure 8. Slip associated with the 2004 earthquake. The slip has been projected onto a planar representation (vertical, striking N40°W) of the nonplanar model geometry for figure clarity. Star marks hypocenter. MM, Middle Mountain; GH, Gold Hill. Plots on left show the slip distribution for the fault surface that intersects the mapped SAF trace. Plots on right show the fault that intersects the SWFZ trace. Upper colorbar corresponds to plots of Figure 8 a-c; lower colorbar corresponds to plot of Figure 8d. (a) Coseismic slip; (b) slip in the first 60 days of the postseismic period; (c) slip during days 60 to 230 of the postseismic period; (d) coseismic slip plus the first 230 days of postseismic.

rounded by aftershocks. To do so, we began with the same fault geometry as in our previous modeling, which included two fault branches above 6 km. Because observations of surface creep suggest that immediate slip occurred along a portion of the SWFZ, while along the main trace the surface displacement was delayed by at least half an hour (Langbein *et al.*, 2006), and in order to fit the coseismic displacement at Carr Hill, we used the secondary branch of the model fault that intersects the SWFZ at the surface rather than the primary branch that intersects the main SAF trace. Below 6 km the fault surface was identical to the main fault used in the results presented in the previous section. We then eliminated the subfaults that fall outside the aftershock zone from the inversion.

The slip distribution inferred using the aftershock-outlined (AO) model (Fig. 9b) has a moment of  $1.0 \times 10^{18}$  N m. The peak slip of 2 m is considerably larger than that estimated by Dreger *et al.* (2004) using a combination of seismic and geodetic data. The fit to the coseismic GPS data using the AO model is poor compared to that using the full fault geometry (Fig. 3b). The variance reduction using the AO model is 83.74%, and only one station (CARH) is fit at 95% confidence. Given uncertainties in the vertical positions of the relocated seismicity, as well as the limitations in approximating the shape and location of the area outlined by aftershocks in terms of triangular subfaults, we also tested a slightly larger AO model that included subfaults that experienced clusters of aftershocks (Fig. 9c). The fit to the data was slightly better than with the more strictly defined AO model (which we will term the “smaller AO model”), particularly at stations HUNT and CANP (Fig. 3c); however the variance reduction was still low (87.52%) relative to that using the full model, and only two stations were fit at 95% confidence.

As reported by Rymer *et al.* (2006) and Langbein *et al.* (2006), there is evidence for surface slip on the SWFZ either coseismically or immediately following the earthquake. Therefore we also tested a scenario in which the coseismic slip occurred in the area outlined by aftershocks, and for 18 km along strike the upper 850 m of the fault also slipped. We used the smaller AO model (Fig. 9b), and included the near-surface subfaults shown in Figure 9d. The resulting slip distribution has a moment of  $1.0 \times 10^{18}$  N m and a peak slip of 1.7 m. The fit to the data (Fig. 3d) is noticeably improved, with a variance reduction of 93.76% and four sites fit at 95% confidence. In particular, near-surface slip is required to fit the data at LAND. The proximity of stations CARH, POMM, and MIDA to the fault makes them sensitive to minor perturbations in geometry. Even with the full fault model, POMM and MIDA (along with HOGS and PKDB) are not fit at 95% confidence. This suggests that the model does not capture the details of the fault geometry and/or the complexities of near-fault deformation that affect these stations.

From these results we conclude that the coseismic GPS displacements cannot be fit by slip confined solely to the area outlined by aftershocks. Near-surface slip can account

for part of the observed signal, but slip between the area outlined by aftershocks and the surface is required to fit some stations' data, given the assumed fault model. One interpretation is that the coseismic rupture of an asperity in the area subsequently outlined by aftershocks continued beyond the locked zone into shallower parts of the fault and triggered slip at the surface. Coseismic slip on the branch of the fault above 6-km depth that intersects the main SAF trace at the surface may also have occurred, contributing to the displacement signal.

As discussed by Waldhauser *et al.* (2004), two prominent streaks of microseismicity beneath Middle Mountain (indicated by arrows in Fig. 6a) coincide with the transition from creeping to locked behavior during the interseismic period inferred from inversion of geodetic data by Murray *et al.* (2001). Figure 6a shows the interseismic long-term average slip-rate distribution estimated from the trilateration, two-color EDM, SGPS, and CGPS data in the present study with relocated seismicity (Waldhauser *et al.*, 2004; Thurber *et al.*, 2006) superimposed. It is notable that the rather abrupt along-strike transition from relatively high to low creep rates occurs within the length of the fault spanned by the streaks. This transition is coincident with the hypocentral region of the 1966 earthquake as well as the three  $M \sim 4.5$ –5 events of the mid-1990s (Fletcher and Spudich, 1998). Compared to the results of Murray *et al.* (2001), the additional geodetic data (i.e., the two-color EDM, post-1999 SGPS, and CGPS measurements) improves resolution in the area above the streak of seismicity at depths of 4 to 8 km between  $-13$  and  $-5$  km along strike. Above 6 km the resolvable length is roughly 9 km along strike and 6 km downdip, and this contracts further at depths of 4 km (Fig. S5 in the electronic edition of BSSA). Although it is not possible to resolve distinct boundaries with geodetic data, the slip distribution in Figure 6a gives a better-resolved image of the transition from creeping to locked behavior than was obtained in previous studies. In particular, the scale of resolvable features above 5 km is roughly the same as the size of the area, characterized by moderate to high slip rate, above and northwest of the upper streak of seismicity. This is consistent with the idea that the fault creeps above the streak in seismicity.

The spatial pattern of interseismic microseismicity between  $-3$  and 20 km along strike (Fig. 6a) is similar to that of aftershocks following the 2004 (and 1966) events (Thurber *et al.*, 2006), suggesting that the fault properties controlling the microearthquake locations exhibit a certain continuity throughout the earthquake cycle. In this context, a self-consistent interpretation is that the seismicity at Parkfield (interseismic and aftershocks) outlines an area of the fault that is interseismically locked (surrounded by areas of the fault that creep) and that ruptured during the most recent earthquake. We conclude that the geodetically imaged low slip rate along this part of the fault is consistent with this interpretation, although the 2004 coseismic slip appears to have extended beyond this zone, perhaps rupturing into areas characterized by aseismic slip.



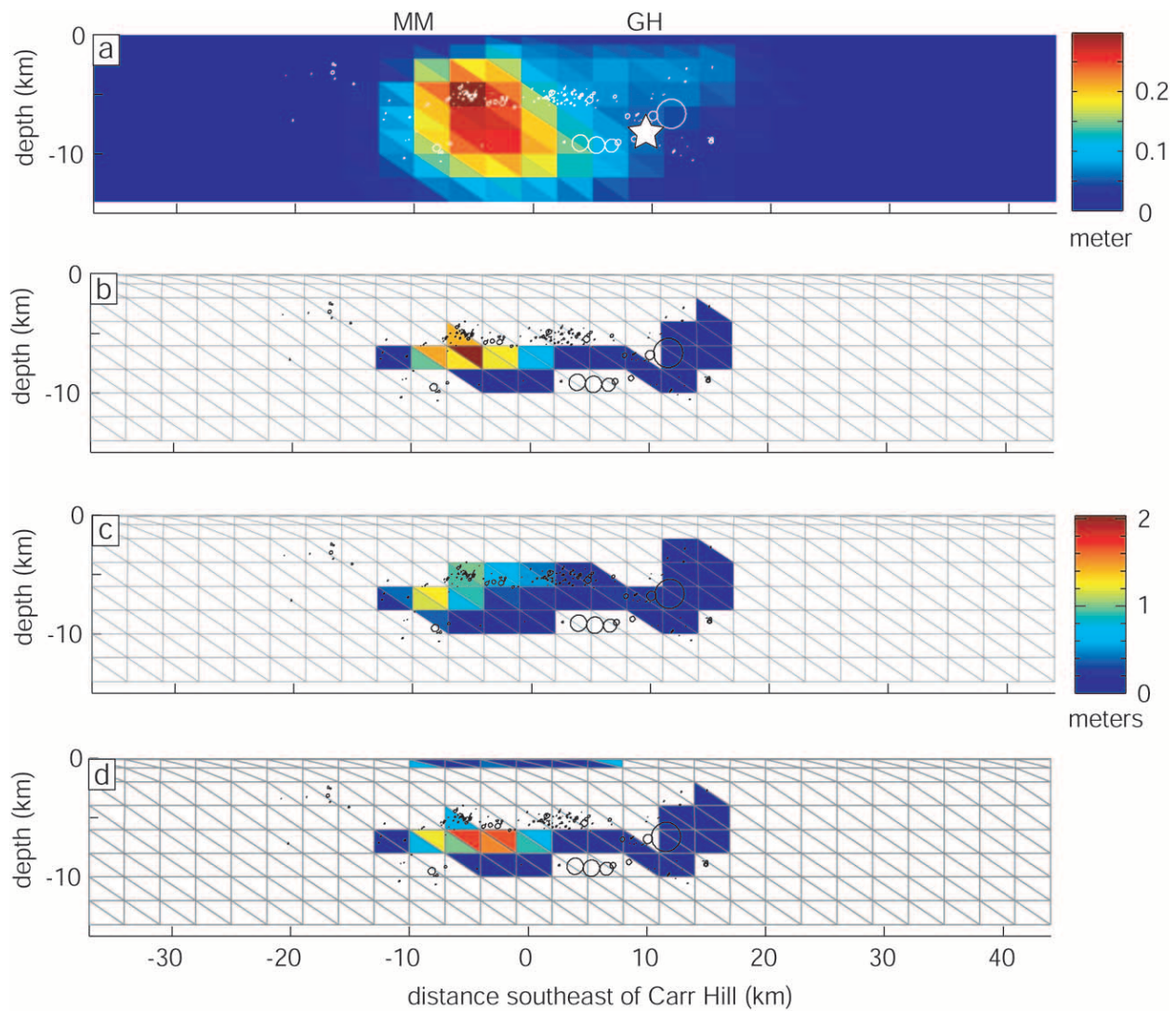


Figure 9. Coseismic slip distributions for the 2004 earthquake (hypocenter indicated by star in top panel) estimated from CGPS data using four different subsets of subfaults. The slip has been projected onto a planar representation (vertical, striking N40°W) of the nonplanar model geometry for figure clarity. Aftershocks occurring within the first day following the earthquake relocated by Thurber *et al.* (2006) are superimposed, plotted as the equivalent rupture area of a 3 MPa stress-drop crack. MM, Middle Mountain; GH, Gold Hill. Upper colorbar applies to Figure 9a; lower colorbar applies to Figure 9b–d. (a) Slip distribution using full fault geometry (identical to Fig. 8a). (b) Slip distribution estimated using only portions of the model fault that are within the area encircled by aftershocks. Uncolored subfaults were not included in the inversion. (c) Slip distribution estimated using portions of the model fault that are within the area encircled by aftershocks or that coincide with clusters of aftershocks. (d) Slip distribution estimated using same subset of subfaults as Figure 9b with the addition of subfaults within 850 m of the Earth's surface in the central portion of the fault. See text for details.

### Is Parkfield Slip-Predictable?

The idea of elastic rebound (Reid, 1910), that stress builds on a fault during the interseismic period, is released in an earthquake, and then reaccumulates until the next event, is an important component of seismic hazard assessment. This concept is embodied in two models for earth-

quake recurrence put forth by Shimazaki and Nakata (1980), termed the time-predictable and slip-predictable models. The former states that the time until the next earthquake on a fault segment is that required to recover the stress released in the most recent event given the interseismic loading rate. Therefore, the bigger the most recent event, the longer until

the next one (assuming constant loading and a fixed failure threshold). In practice, the predicted recurrence time is calculated as the ratio of coseismic moment release to interseismic moment deficit rate. The slip-predictable model states that the size of an upcoming earthquake can be forecast from the rate of interseismic loading and the time since the most recent event. The longer since the last earthquake, the bigger the next one will be. The size may be calculated from the product of moment deficit rate and the elapsed time since the most recent earthquake.

Murray and Segall (2002) showed, using geodetic data, that the time-predictable model did not accurately forecast a subsequent earthquake on the 1966 Parkfield earthquake rupture plane. With the occurrence of the 2004 event it is possible to address the question of whether Parkfield is slip predictable. As part of their 2002 study, Murray and Segall, estimated a probability distribution of moment deficit rates on the San Andreas for the interseismic period after 1966 using a fault model that extended from 16 km northwest to 23 km southeast of Carr Hill. For a range of times, we used the upper and lower 95% confidence limits from Murray and Segall's (2002) distribution of moment deficit rates to calculate the size of the Parkfield earthquake that would be expected according to the slip-predictable model (solid and dashed black lines on Fig. 10). Based on this model, the distribution of moment deficit rates would allow a large range of moments for an earthquake at Parkfield in 2004.

The length of the fault for which Murray and Segall (2002) estimated the distribution of moment deficit rates was based on the inferred extent of the 1966 earthquake slip. In order to compare the moment release in the 2004 earthquake to that expected based on the slip-predictable model, we consider only the length of the 2004 rupture that coincides with that of Murray and Segall's (2002) study. This captures essentially all slip to the southwest of the 2004 hypocenter but neglects some deep postseismic slip to the northwest (e.g., Fig. 8d). However, this slip makes a negligible contribution to the total moment release and is on a poorly resolved part of the fault.

The estimated moment release associated with the 2004 earthquake, including the first 230 days of the postseismic period, does not fall within the slip-predictable range (black star, Fig. 10). By fitting a logarithmic decay function to the postseismic geodetic data, Langbein *et al.* (2006) estimate that after 230 days, 47% of the postseismic deformation has occurred, with an interquartile range of 38%–60%. If this is true, given the estimated slip in the 2004 earthquake and during the first 230 days of the postseismic period along the portion of the fault considered here, the total moment release will be  $6.8 \times 10^{18}$  N m ( $8.1 \times 10^{18}$  N m if only 38% of the postseismic signal has occurred thus far, shown as the white star on Fig. 10). This value is still not within the 95% confidence limits on the slip-predictable moment.

Recent paleoseismological evidence suggests that the time- and slip-predictable models poorly describe the occurrence of large earthquakes over many earthquake cycles

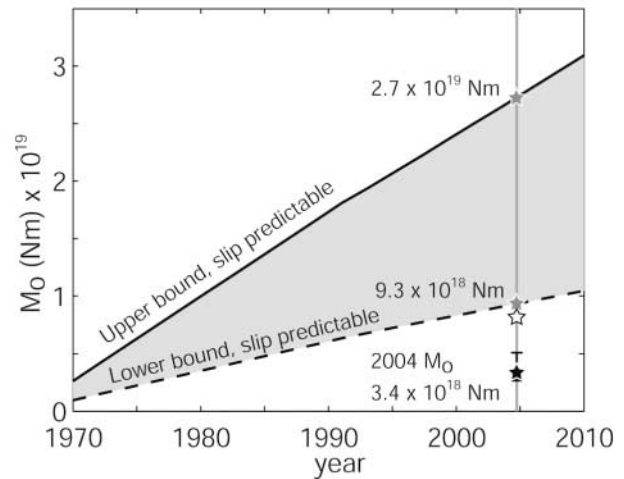


Figure 10. Range of expected moment release based on the slip-predictable model. The upper and lower 95% confidence limits on moment deficit rate for the portion of the fault from 16 km northwest to 23 km southeast of Carr Hill were obtained from the probability distribution of moment deficit rates estimated by Murray and Segall (2002). These moment deficit rates were used to calculate the predicted moment for a range of elapsed times, indicated by the shaded region. At the time of the 2004 earthquake (vertical gray line) the expected range of moment release according to the slip-predictable model was  $9.3 \times 10^{18}$  N m to  $2.7 \times 10^{19}$  N m (indicated by gray stars). The estimated moment release along the same portion of the fault during the coseismic and first 230 days of the postseismic period for the 2004 earthquake was  $3.4 \times 10^{18}$  N m (black star with  $2\sigma$  error bar based on bootstrap calculations), below the slip-predictable range. The white star is the projected total moment release if the first 230 days of the postseismic period represent 38% of the total postseismic moment release.

spanning thousands of years (Weldon *et al.*, 2004; Hubert-Ferrari *et al.*, 2005). Rather, the events appear to cluster in time, suggesting alternating periods of rapid strain release and relative quiet. In such a situation, temporal clusters of earthquakes may release strain accumulated over a considerably longer time, and a net surplus of strain accumulates during the periods without frequent large earthquakes (Weldon *et al.*, 2004).

#### Progression of Slip along the Fault over Time

Another difficulty in applying the simple recurrence models discussed previously is that they assume repeated rupture of the same fault segment and complete release of stored stress on the fault during an earthquake. Some paleoseismological investigations have concluded that, at least in great earthquakes, the rupture length is relatively constant (Liu *et al.*, 2004). However, inspection of the slip distributions for the three most recent Parkfield earthquakes (Fig. 5)

shows that even with the addition of postseismic slip, the 2004 earthquake slip distribution does not mimic that of 1966 but rather is more similar in extent to that in 1934. While it is difficult given the sparse data for 1966 to rule out that the 1966 and 2004 events were significantly different between Middle Mountain and Carr Hill, the bootstrap analysis indicates there was significantly more slip southeast of Gold Hill in the 1966 event. Even if earthquakes are not time or slip predictable, it is reasonable to assume that over sufficiently long time intervals the seismogenic fault must keep up with the long-term displacement across it. Thus, it is conceivable that the somewhat complementary slip distributions of successive Parkfield events would, over multiple earthquake cycles, achieve uniform release of strain along the 60 km of the San Andreas near Parkfield.

To investigate how slip evolves along the fault over two earthquake cycles and where there are gaps in slip yet to be filled, we calculated the spatial distribution of cumulative fault slip since the 1934 earthquake (Fig. 11). There are insufficient geodetic data to estimate the interseismic slip-rate distribution along the fault between 1934 and 1966, so we assumed that the slip-rate distribution was the same as the long-term average slip rate estimated for 1966–2004. For the 1966–2004 period, the slip-rate distribution used in the calculation includes the estimated transient change in slip rate. We do not know if earlier transient deformation events have occurred at Parkfield, but in 20 years of quasi-continuous monitoring only one such episode has been observed. This suggests that the contribution of transient increases in slip rate to the total slip budget is small. On the right side of Figure 11 (plots e, f, and g) the maximum value on the color scale is the amount of cumulative slip that would be expected if the fault slipped at the long-term rate of 33 mm/yr (Murray *et al.*, 2001); areas with warm colors have less accumulated slip deficit.

In order to assess the uncertainties on the estimated cumulative slip distribution we use the 1000 realizations of each of the slip distributions shown Figure 11a–d obtained from the bootstrap. Following Murray and Segall (2002), we randomly draw a slip or slip-rate distribution from the set of bootstrap solutions for each of the four time intervals. We then sum these to obtain a cumulative slip distribution. This procedure is repeated to produce 1000 realizations of the cumulative slip from which the 95% confidence interval can be obtained. These are shown in terms of slip deficit assuming a long-term slip rate of 33 mm/yr in Figure 12.

The long-term slip rate, on which the slip deficit depends, is not known precisely, and values estimated from geodetic data are model dependent. For instance a solution found using a shallower transition depth will have a lower estimated long-term slip rate. Murray *et al.* (2001) found that the combination of 14 km and 33 mm/yr was the best fit to the SGPS data. The transition depth we use in this study, 14 km, is consistent with the depth distribution of seismicity at Parkfield. Based on observations at Wallace Creek, southeast of Parkfield, the geologically estimated long-term slip

rate is  $33.9 \pm 2.9$  mm/yr (Sieh and Jahns, 1984). Therefore, we consider the assumption of 33 mm/yr as the long-term slip rate to be a reasonable choice in the following discussion.

As can be seen from Figure 11, the 1966 and 2004 earthquakes contribute relatively little to the reduction of slip deficit, whereas the ongoing interseismic creep prevents the northwestern  $\sim 30$  km of the fault from developing a slip deficit since the 1934 earthquake. The geodetic observations require that the fault slipped between Carr Hill and Gold Hill during the two most recent earthquakes. However, between those two locations the median slip deficit is  $1.4 \pm 0.18$  m at 95% confidence. Along the Carr Hill–Gold Hill stretch nearly the entire fault surface from 4- to 12-km depth has at least 1 m of slip deficit at 95% confidence (Fig. 12). Harris and Archuleta (1988) came to a similar conclusion under the assumption that all Parkfield earthquakes were comparable to the 1966 event. That the fault is capable of partially releasing stored strain in a moderate earthquake, maintaining a disequilibrium through multiple earthquake cycles, is problematic for the application of simple recurrence models that depend on the idea that only the strain accumulated since the most recent event is relevant to the upcoming earthquake. At Parkfield the moment deficit accumulated between  $M$  6.0 earthquakes predicts neither the time nor the size of the upcoming event well. It appears a combination of  $M$  6.0 earthquakes, larger less frequent events, and interseismic creep are necessary for the fault at Parkfield to keep up with the long-term slip.

During the 1934–2004 period alone the median slip deficit over the 33 km southeast of Gold Hill is  $2.0 \pm 0.15$  m at 95% confidence. This corresponds to a moment deficit of  $6.0 \times 10^{18}$  N m, equivalent to an  $M_w$  6.5 event over that length of the fault. These results are in keeping with earlier work (Sieh and Jahns, 1984; Harris and Archuleta, 1988; Arrowsmith *et al.*, 1997), which concluded that slip deficit southeast of the Parkfield region left that portion of the fault, which last ruptured in the 1857 Fort Tejon earthquake, vulnerable to a future large event ( $\sim M$  7). These studies all postulated that the Parkfield earthquake subsequent to 1966 would rupture a greater length of the fault, extending perhaps  $\sim 40$  km southeast of Gold Hill, or would trigger a separate event on the Cholame and/or Carrizo segments. Despite the accumulated slip deficit southeast of Gold Hill and the stress increase to which this part of the fault was subjected due to the 2004 earthquake, to date such a scenario has not taken place. This further emphasizes that accumulated slip deficit is not sufficient for earthquake nucleation.

The study of strain accumulation and release presented here highlights one significant feature of the earthquake cycle at Parkfield: the apparent tendency of the Middle Mountain to Cholame segment of the SAF to rupture in both moderate and large earthquakes. This may be due in part to the transitional nature of this stretch of the fault and its location at the edge of the locked section to the southeast. The persistence of slip deficit through multiple moderate earth-



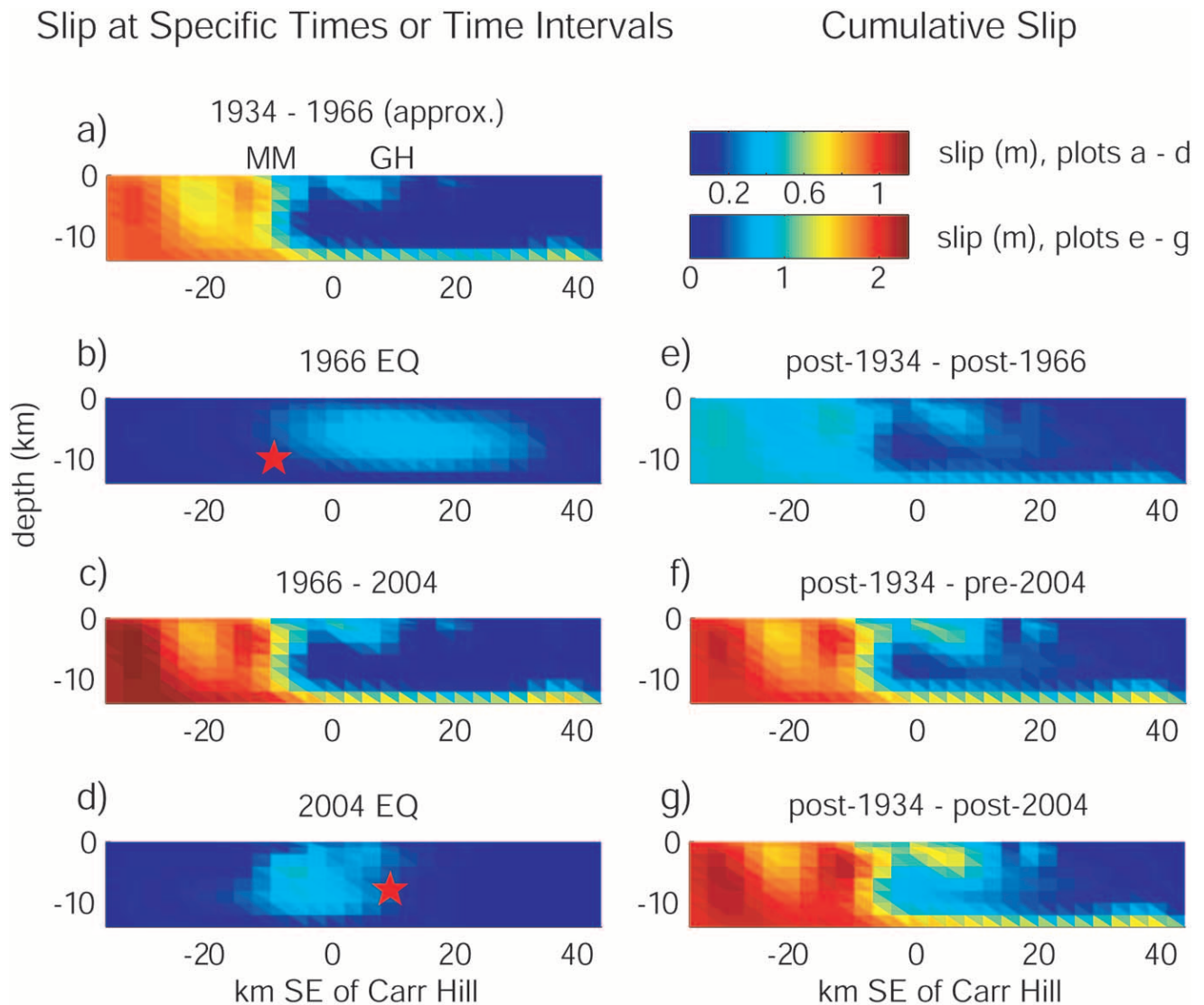


Figure 11. Progression of slip on the SAF at Parkfield since the 1934 earthquake. The slip has been projected onto a planar representation (vertical, striking  $N40^{\circ}W$ ) of the nonplanar model geometry for figure clarity. Figure 11a–d show slip at specified time intervals, and Figure 11e–g show the cumulative sum of the estimated slip. (a) Cumulative interseismic slip between 1934 and 1966 assuming that the interseismic slip-rate distribution is comparable to that between 1966 and 2004; MM, Middle Mountain; GH, Gold Hill; (b) Slip in the 1966 earthquake; star is hypocenter; (c) Cumulative interseismic slip between 1966 and 2004 including the estimated slip-rate change between 1993 and 1996; (d) Slip in the 2004 earthquake and first 230 days of the post-seismic period; star is hypocenter. Slip on the primary and subsidiary fault surfaces has been summed. (e) The cumulative slip starting after the 1934 earthquake until after the 1966 earthquake (sum of Fig. 11 a and b); (f) Cumulative sum of slip starting after the 1934 earthquake until just before the 2004 event (sum of Fig. 11a–c); (g) Cumulative sum from after the 1934 earthquake until April 2005 (sum of Fig. 11a–d). Figure 11a–d use a different color scale from Figure 11e–g. For Figure 11e–g the maximum value on the color scale is the slip that would be expected if the whole fault slipped at the long-term rate of 33 mm/yr.

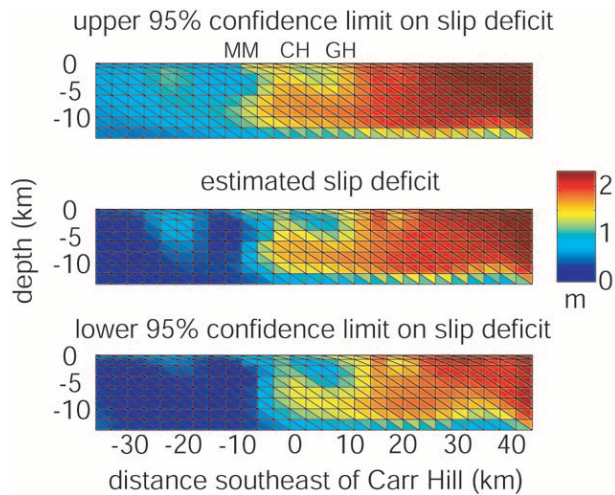


Figure 12. The lower and upper 95% confidence limits on the best-fitting cumulative slip deficit (relative to a long-term slip rate of 33 mm/yr) obtained using bootstrap resampling for each subfault. The slip has been projected onto a planar representation (vertical, striking N40°W) of the nonplanar model geometry for figure clarity. Between Carr Hill (CH) and Gold Hill (GH) the entire fault surface from 4- to 12-km depth has at least 1m of slip deficit at 95% confidence. MM, the along-strike location of Middle Mountain.

quakes is also another manifestation of the variable rates of strain accumulation and release that Weldon *et al.* (2004) observed in the paleoseismologic record for large earthquakes in southern California, where evidence exists for temporal clustering of events.

Other factors also contribute to the complexity of the earthquake cycle at Parkfield. Nearby earthquakes like the 1983 *M* 6.7 Coalinga and 2003 *M* 6.5 San Simeon events, long-term postseismic effects such as viscoelastic relaxation of the lower crust, and transient slip-rate accelerations can contribute to temporal variations in the stressing rate. Although the transient slip at Parkfield makes a small contribution to the accumulated slip, locally the stress changes it caused may have been influential given its proximity to the nucleation zone of the 1934 and 1966 earthquakes.

### Conclusions

Joint inversion of a variety of geodetic data collected in the Parkfield region has produced a higher resolution image of the spatial distribution of interseismic slip rate along the fault than was previously available. The geodetically imaged transition from regions experiencing long-term interseismic creep to essentially locked behavior beneath Middle Mountain is within the resolving power of the data at spatial scales of 6–9 km. This transition occurs within a zone spanned by two streaks of microseismicity that have persisted over decades and perhaps through multiple *M* 6.0 earthquakes (Wald-

hauser *et al.*, 2004). The displacement of the continuous GPS site at Carr Hill during and after the 2004 earthquake is consistent with slip on multiple subparallel fault strands, and a branching fault structure is apparent in the relocated aftershock distribution. In locales like Parkfield, where geodetic stations are located close to the fault, the aftershock locations can provide useful information for developing more representative models of fault geometry. This may become more important as continuous GPS networks densify near-fault monitoring. Although the postseismic slip following the Parkfield earthquake represents more than twice the moment release of the coseismic slip, the total moment release after 230 days still does not put the 2004 Parkfield earthquake within the slip-predictable range of moments. The primary means of strain release on the San Andreas near Parkfield since 1934 has been interseismic creep along the northwestern 30 km of the fault. The median slip deficit on the 33 km southeast of Gold Hill since 1934 alone is 2 m, capable of producing a *M<sub>w</sub>* 6.5 event.

### Acknowledgments

We wish to thank Robert Simpson for creating the fault geometry based on aftershock locations. We also thank Matthew d'Alessio, Ingrid Johanson, Eric Fielding, and Robert Simpson for useful comments and suggestions. We are indebted to the numerous people who, over the years, maintained the geodetic networks and collected the data used in this study. This research was funded, in part, by the USGS Mendenhall Postdoctoral Fellowship Program.

### References

- Arrowsmith, R., K. McNally, and J. Davis (1997). Potential for earthquake rupture and *M*7 earthquakes along the Parkfield, Cholame, and Carrizo Segments of the San Andreas fault, *Seism. Res. Lett.* **68**, 902–916.
- Bakun, W. H., and A. G. Lindh (1985). The Parkfield, California, earthquake prediction experiment, *Science* **229**, 619–624.
- Bakun, W., B. Aagaard, B. Dost, W. L. Ellsworth, J. L. Hardebeck, R. A. Harris, C. Ji, M. J. S. Johnston, J. Langbein, J. J. Lienkaemper, A. J. Michael, J. R. Murray, R. M. Nadeau, P. A. Reasenberg, M. S. Reichle, E. A. Roeloffs, A. Shakal, R. W. Simpson, and F. Waldhauser (2005). Implications for prediction and hazard assessment from the 2004 Parkfield earthquake, *Nature* doi 10.1038/nature04067.
- Boucher, C., Z. Altamimi, P. Sillard, and M. Feissel-Vernier (2004). *The ITRF2000, IERS Technical Note 31*, Verlag des Bundesamts für Kartographie und Geodäsie, Frankfurt, 289 pp.
- Brown, R., Jr., J. Vedder, R. Wallace, E. Roth, R. Yerkes, R. Castle, A. Waananen, R. Page, and J. Eaton (1967). The Parkfield-Cholame, California earthquakes of June–August 1966: surface geologic effects, water-resources aspects, and preliminary seismic data., *U.S. Geol. Surv. Prof. Pap.* **579**, 66 pp.
- Burford, R., and P. Harsh (1980). Slip on the San Andreas fault in central California from alignment array surveys, *Bull. Seism. Soc. Am.* **70**, 1233–1261.
- Comninou, M., and J. Dundurs (1975). The angular dislocation in a half space, *J. Elasticity* **5**, 203–216.
- Desbrun, M., M. Meyer, P. Schroder, and A. Barr (1999). Implicit fairing of irregular meshes using diffusion and curvature flow, in *SIGGRAPH 99 Conference Proceedings*, Addison Wesley Professional, Boston, 317–324.
- Dreger, D., M. Murray, and D. Oglesby (2004). Kinematic modeling of the

- 2004 Parkfield earthquake, *EOS Trans. AGU* **85**, Fall Meet. Suppl., Abstract S51C-01701.
- Du, Y., A. Aydin, and P. Segall (1992). Comparison of various Inversion techniques as applied to the determination of a geophysical deformation model for the 1983 Borah Peak earthquake, *Bull. Seism. Soc. Am.* **82**, 1840–1866.
- Efron, B., and R. J. Tibshirani (1993). *An Introduction to the Bootstrap: Monographs on Statistics and Applied Probability*, Vol. 57, Chapman and Hall, New York.
- Fletcher, J., and P. Spudich (1998). Rupture characteristics of the three M ~4.7 (1992–1994) Parkfield earthquakes, *J. Geophys. Res.* **103**, 835–854.
- Gao, S., P. Silver, and A. Linde (2000). A comprehensive analysis of deformation data at Parkfield, California: detection of a long-term strain transient, *J. Geophys. Res.* **105**, 2955–2967.
- Gwyther, R., M. Gladwin, M. Mee, and R. H. G. Hart (1996). Anomalous shear strain at Parkfield during 1993–94, *Geophys. Res. Lett.* **23**, 2425–2428.
- Hardebeck, J. L., J. Boatwright, D. Dreger, R. Goel, V. Graizer, K. Hudnut, C. Ji, L. Jones, J. Langbein, J. Lin, E. Roeloffs, R. Simpson, K. Stark, R. Stein, and J. C. Tinsley (2004). Preliminary Report on the 22 December 2003 M6.5 San Simeon, California, Earthquake, *Seism. Res. Lett.* **75**, 155–172.
- Harris, R., and R. Archuleta (1988). Slip budget and potential for a M7 earthquake in Central California, *Geophys. Res. Lett.* **15**, 1215–1218.
- Harris, R. A., and P. Segall (1987). Detection of a locked zone at depth on the Parkfield, California segment of the San Andreas fault, *J. Geophys. Res.* **92**, 7945–7962.
- Hubert-Ferrari, A., J. Suppe, J. Van Der Woerd, X. Wang, and H. Lu (2005). Irregular earthquake cycle along the southern Tianshan front, Aksu area, China, *J. Geophys. Res.* **110**, doi 10.1029/2003JB002603.
- King, N., P. Segall, and W. Prescott (1987). Geodetic measurements near Parkfield, California, 1959–1984, *J. Geophys. Res.* **92**, 2747–2766.
- Langbein, J. (2004). Noise in two-color electronic distance meter measurements revisited, *J. Geophys. Res.* **109**, doi 10.1029/2003JB002819.
- Langbein, J., and Y. Bock (2004). High-rate real-time GPS network at Parkfield: utility for detecting fault slip and seismic displacements, *Geophys. Res. Lett.* **31**, doi 10.1029/2003GL019408.
- Langbein, J., and H. Johnson (1997). Correlated errors in geodetic time series: implications for time-dependent deformation, *J. Geophys. Res.* **102**, 591–603.
- Langbein, J., R. Burford, and L. Slater (1990). Variations in fault slip and strain accumulation at Parkfield, California: initial results using two-color geodimeter measurements, 1984–1988, *J. Geophys. Res.* **95**, 2533–2552.
- Langbein, J., R. L. Gwyther, R. H. G. Hart, and M. T. Gladwin (1999). Slip-rate increase at Parkfield in 1993 detected by high-precision EDM and borehole tensor strainmeters, *Geophys. Res. Lett.* **26**, 2529–2532.
- Langbein, J., M. Linker, A. McGarr, and L. Slater (1987). Precision of two-color geodimeter measurements: results from 15 months of observations, *J. Geophys. Res.* **92**, 11,644–11,656.
- Langbein, J., J. Murray, and H. A. Snyder (2006). Coseismic and initial postseismic deformation from the 2004 Parkfield, California earthquake, observed by Global Positioning System, creepmeters, and borehole strainmeters, *Bull. Seism. Soc. Am.* **96**, no. 4B, S304–S320.
- Langbein, J., R. Borchardt, D. Dreger, J. Fletcher, J. L. Hardebeck, M. Hellweg, C. Ji, M. Johnston, J. R. Murray, R. Nadeau, M. J. Rymer, and J. A. Treiman (2005). Preliminary report on the 28 September 2004, M6.0 Parkfield, California, earthquake, *Seism. Res. Lett.* **76**, 1–17.
- Lienkaemper, J. J., and W. H. Prescott (1989). Historic surface slip along the San Andreas fault near Parkfield, California, *J. Geophys. Res.* **94**, 17,647–17,670.
- Lienkaemper, J. J., B. Baker, and F. McFarland (2006). Surface slip associated with the 2004 Parkfield, California, earthquake measured on alignment arrays, *Bull. Seism. Soc. Am.* **96**, no. 4B, S239–S249.
- Lisowski, M., and W. H. Prescott (1981). Short-range distance measurements along the San Andreas fault system in central California, 1975 to 1979, *Bull. Seism. Soc. Am.* **71**, 1607–1624.
- Liu, J., Y. Klinger, K. Sieh, and C. Rubin (2004). Six similar sequential ruptures of the San Andreas fault, Carrizo Plain, California, *Geology* **32**, doi 10.1130/G20478.1.
- Maerten, F., P. Resor, D.D. Pollard, and L. Maerten (2005). Inverting for slip on three-dimensional fault surfaces using angular dislocations, *Bull. Seism. Soc. Am.* **95**, 1654–1665, doi 10.1785/0120030181.
- Manaker, D., R. Burgmann, W. Prescott, and J. Langbein (2003). Distribution of interseismic slip rates and the potential for significant earthquakes on the Calaveras fault, central California, *J. Geophys. Res.* **108**, doi 10.1029/2002JB001749.
- Mendoza, C., and S. Hartzell (1988). Aftershock patterns and main shock faulting, *Bull. Seism. Soc. Am.* **78**, 1438–1449.
- Murray, J. R., and P. Segall (2002). Testing time-predictable earthquake recurrence by direct measure of strain accumulation and release, *Nature* **419**, 287–291.
- Murray, J., and P. Segall (2005). Spatiotemporal evolution of a transient slip event on the San Andreas Fault near Parkfield, California, *J. Geophys. Res.* **110**, doi 10.1029/2005JB003651.
- Murray, J. R., P. Segall, P. Cervelli, W. Prescott, and J. Svarc (2001). Inversion of GPS data for spatially variable slip-rate on the San Andreas fault near Parkfield, California, *Geophys. Res. Lett.* **28**, 359–362.
- Okada, Y. (1985). Surface deformation due to shear and tensile faults in a half-space, *Bull. Seism. Soc. Am.* **75**, 1135–1154.
- Oppenheimer, D., W. Bakun, and A. Lindh (1990). Slip partitioning of the Calaveras Fault, California, and prospects for future earthquakes, *J. Geophys. Res.* **95**, 8483–8498.
- Prescott, W. H. (1976). An extension of Frank's method for obtaining crustal shear strains from survey data, *Bull. Seism. Soc. Am.* **66**, 1847–1853.
- Reid, H. (1910). The mechanics of the earthquake: the California earthquake of April 18, 1906, Report of the State Earthquake Investigation Commission, Vol. 2, Carnegie Institution of Washington, Washington, D.C., 192 pp.
- Roeloffs, E. (2001). Creep rate changes at Parkfield, California, 1966–1999: seasonal, precipitation induced, and tectonic, *J. Geophys. Res.* **106**, 16,525–16,547.
- Rymer, M. J., J. C. Tinsley, J. A. Treiman, J. R. Arrowsmith, K. B. Clahan, A. M. Rosinski, W. A. Bryant, H. A. Snyder, G. S. Fuis, N. A. Toké, and G. W. Bawden (2006). Surface fault slip associated with the 2004 Parkfield, California, earthquake, *Bull. Seism. Soc. Am.* **96**, no. 4B, S11–S27.
- Savage, J. C. (1990). Equivalent strike-slip earthquake cycles in half-space and lithosphere-asthenosphere Earth models, *J. Geophys. Res.* **95**, 4873–4879.
- Schaff, D., G. Bokelmann, G. Beroza, F. Waldhauser, and W. Ellsworth (2002). High-resolution image of Calaveras Fault seismicity, *J. Geophys. Res.* **107**, doi 10.1029/2001JB000633.
- Schwartz, D., and K. Coppersmith (1984). Fault behavior and characteristic earthquakes: examples from the Wasatch and San Andreas fault zones, *J. Geophys. Res.* **89**, 5681–5698.
- Segall, P., and Y. Du (1993). How similar were the 1934 and 1966 Parkfield earthquakes? *J. Geophys. Res.* **98**, 4527–4538.
- Segall, P., and R. Harris (1987). Earthquake deformation cycle on the San Andreas fault near Parkfield, California, *J. Geophys. Res.* **92**, 10,511–10,525.
- Shimazaki, K., and T. Nakata (1980). Time-predictable recurrence model for large earthquakes, *Geophys. Res. Lett.* **7**, 279–282.
- Sieh, K. E. (1978). Slip along the San Andreas Fault associated with the great 1857 earthquake, *Bull. Seism. Soc. Am.* **68**, 1421–1447.
- Sieh, K., and R. Jahns (1984). Holocene activity of the San Andreas Fault at Wallace Creek, California, *Geol. Soc. Am. Bull.* **95**, 883–896.
- Smith, S., and M. Wyss (1968). Displacement on the San Andreas fault subsequent to the 1966 Parkfield earthquake, *Bull. Seism. Soc. Am.* **58**, 1955–1973.



- Thurber, C., H. Zhang, F. Waldhauser, J. Hardebeck, A. Michael, and D. Eberhart-Phillips (2006). Three-dimensional compressional wave-speed model, earthquake relocations, and focal mechanisms for the Parkfield, California, region, *Bull. Seism. Soc. Am.* **96**, no. 4B, S38–S49.
- Titus, S., C. DeMets, and B. Tikoff (2005). New slip rate estimates for the creeping segment of the San Andreas fault, California, *Geology* **33**, 205–208.
- Wahba, G. (1990). *Spline Models for Observational Data*, Society for Industrial and Applied Mathematics, Philadelphia.
- Waldhauser, F., W. L. Ellsworth, D. P. Schaff, and A. Cole (2004). Streaks, multiplets, and holes: high-resolution spatio-temporal behavior of Parkfield seismicity, *Geophys. Res. Lett.* **31**, L18608, doi 10.1029/2004GL020649.
- Weldon, R., K. Scharer, T. Fumal, and G. Biasi (2004). Wrightwood and the earthquake cycle: what a long recurrence record tells us about how faults work, *GSA Today* **14**, doi 10.1130/1052-5173(2004)014<4:WATECW>2.0.CO;2.
- Yu, E., and P. Segall (1996). Slip in the 1868 Hayward earthquake from the analysis of historical triangulation data, *J. Geophys. Res.* **101**, 16,101–16,118.
- Zumberge, J. F., M. B. Heflin, D. C. Jefferson, M. M. Watkins, and F. H. Webb (1997). Precise point positioning for the efficient and robust analysis of GPS data from large networks, *J. Geophys. Res.* **102**, 5005–5017.

U.S. Geological Survey  
345 Middlefield Road, MS 977  
Menlo Park, California 94025  
jrmurray@usgs.gov

Manuscript received 19 September 2005.